

Electronic Supplementary Information for

Stereoretention in styrene heterodimerisation promoted by one-electron oxidants

Xinglong Zhang,^{1,3} and Robert S. Paton,^{1,2*}

¹ Department of Chemistry, Chemistry Research Laboratory, University of Oxford, Mansfield Road, Oxford, OX1 3TA, UK

² Department of Chemistry, Colorado State University, Fort Collins, CO 80523, USA

³ Present address: Division of Chemistry and Chemical Engineering, California Institute of Technology, Pasadena, California 91125, USA

Email: robert.paton@colostate.edu

Table of Contents

1. Computational methods	S2
2. Computational electrochemical potential benchmarking	S3
2.1 Conformational considerations for Dess-Martin periodinane (DMP), hexafluoroisopropanol (HFIP) and DMP-HFIP complex	S5
3. Reaction P1 (<i>trans</i> -anethole + <i>trans</i> - β -methylstyrene)	S6
4. Reaction P2 (<i>trans</i> -anethole + <i>cis</i> - β -methylstyrene)	S16
5. Estimate of electron transfer barrier	S27
6. Absolute contributions to Gibbs energy	S34
7. Optimised geometries	S38
8. References	S38

1. Computational methods

DFT calculations were performed with *Gaussian 09* rev. D.01.¹ Geometry optimisations were carried out using the hybrid meta-GGA functional M06-2X² within the unrestricted formalism using the Unrestricted Kohn-Sham (UKS) theory, with the Pople-type double- ζ split-valence basis set 6-31G(d).³ For the hypervalent iodine oxidant, a mixed basis set of LANL2DZ⁴ for the Iodine atom and the 6-31G(d) basis set for all other atoms was used. Minima and transition structures on the potential energy surface (PES) were confirmed as such by harmonic frequency analysis at the same level of theory. Intrinsic reaction coordinate (IRC)^{5,6} analyses were carried out to connect the proposed TS structures to correct minima. The eigenvalues of the spin operator S^2 after annihilation of spin contamination were found to range from 0.750 to 0.751 for all radical cationic structures, in agreement with the expected value of $S(S+1) = 0.75$ for a doublet wavefunction, indicating that spin contamination is not a problem for the present methodology. Single point corrections were carried out with M06-2X functional using the Karlsruhe-family polarised triple- ζ def2-TZVPP basis set.⁷⁻⁹

The SMD continuum solvation model¹⁰ was included to account for the effect of implicit solvents acetonitrile (MeCN) and hexafluoroisopropanol (HFIP) on the computed Gibbs energy profile. HFIP is a versatile solvent in organic synthesis, especially in its role in stabilising radical cations¹¹⁻¹³ and promoting single electron oxidation when combined with hypervalent iodine reagents^{12,14}, making its computational parametrisation within the SMD model important for general use. Since HFIP solvent is not available in the list of default/pre-defined solvents in *Gaussian 09* software, it is herein parametrised using a set of seven parameters.¹⁰ These include the static dielectric constant of the solvent at 25°C ($Eps = 16.7$),^{13,15,16} dynamic (optical) dielectric constant – the square of the refractive index value of 1.275 at 20°C was used¹⁷ ($EpsInf = 1.625625$); hydrogen bond acidity ($HBondAcidity = 1.96$) and basicity ($HBondBasicity = 0.00$),¹³ which are Abraham's *A* and *B* values respectively; the surface tension of the solvent at interface ($SurfaceTensionAtInterface = 23.23$);^{18,19} carbon aromaticity – the fraction of aromatic carbons ($CarbonAromaticity = 0.00$) and electronegative halogenicity – the fraction of halogens ($ElectronegativeHalogenicity = 0.60$). These parameters were specified using the keyword “SCRF = (SMD, Solvent= Generic, Read)” in *Gaussian 09*.

All Gibbs energies were evaluated at 313.15K and were corrected for zero-point vibrational energies at the same level of theory. These values were further corrected by applying the quasi-rigid rotor harmonic oscillator (quasi-RRHO) for the vibrational entropies, as described by Grimme,²⁰ using a free-rotor approximation for anharmonic vibrational modes below 100 cm⁻¹ and a rigid rotor harmonic oscillator approximation above this wavenumber.²¹ The free energies were further corrected using a standard concentration of 1 mol L⁻¹, which was used in solvation calculations. The solvent-corrected SMD(HFIP)-UM06-2X/def2-TZVPP// UM06-2X/6-31G(d) values are used for discussion.

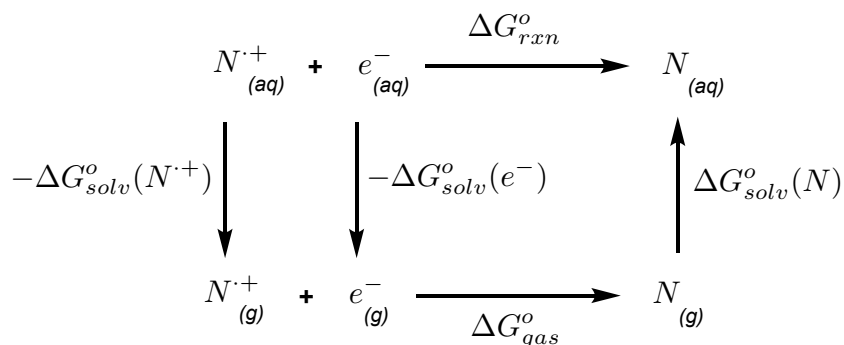
Energy decomposition analyses were performed every three steps along the IRC up to the transition structures using the second-generation ALMO-EDA method²² implemented in Q-Chem.²³ The total interaction energy was decomposed into Pauli repulsion (E_{Pauli}), electrostatics (E_{elec}), dispersion (E_{disp}), charge-transfer and polarization terms (these last two are collected and reported as E_{orb}). These calculations were performed at the M06-2X/def2-TZVP level of theory, with a (99, 590) integration grid.

Non-covalent interactions (NCIs) were analysed using NCIPLLOT²⁴ calculations. The *.wfn* files for NCIPLLOT were generated at M06-2X/6-31G(d) level of theory. NCI indices calculated with NCIPLLOT were visualised at a gradient isosurface value of $s = 0.5$ au. These are coloured according to the sign of the second eigenvalue (λ_2) of the Laplacian of the density ($\nabla^2\rho$) over the range of -0.1 (blue = attractive) to +0.1 (red = repulsive). Molecular orbitals are visualised using an isosurface value of 0.05 a.u. throughout.

Molecular structures, non-covalent interaction plots and spin density plots were visualised using PyMol software.²⁵ *Unless otherwise stated, all energy values are quoted in kcal mol⁻¹ and bond distances in Å.*

2. Computational electrochemical potential benchmarking

To calculate the electrochemical redox potential, we need to calculate the overall Gibbs energy of reaction in solvent, ΔG_{rxn}^o as shown in Scheme 1. One can either a) directly calculate the reaction energies within continuum solvation models, i.e., direct geometry optimisations of both neutral and radical cationic species in the solution phase, or b) construct a thermodynamic cycle by separate gas phase geometry optimisations with single point solvation energy of each species.



Scheme S1. Computation of redox potential for the reduction of a radical cation to its neutral form.

We use a thermodynamic cycle here to express ΔG_{rxn}^o in terms of the free energy of reaction in gas phase, ΔG_{gas}^o and the free energies of solvation, ΔG_{solv}^o of the reacting species as shown.^{26,27} Since the differences in the redox potentials obtained from both direct and thermodynamic cycle methods are very small when solvent-induced geometry changes are small (for example, no change in protonation state upon solvation),²⁶ we adopt the thermodynamic cycle approach here.

In our calculations, the gas phase energy change, ΔG_{gas}^o is further refined by calculating the single point energy in gas-phase at a larger basis set (def2-TZVPP) for improved accuracy.²⁶ The reduction potentials calculated here are *adiabatic* reduction potentials (ARP) since the energy is taken from each optimised species, i.e.,

$$\text{ARP} = E(\text{optimised neutral}) - E(\text{optimised radical cation}). \quad (1)$$

We then have

$$\Delta G_{rxn}^o = -\Delta G_{solv}^o(N^{\bullet+}) - \Delta G_{solv}^o(e^-) + \Delta G_{gas}^o(N^{\bullet+}) + \Delta G_{solv}^o(N) \quad (2)$$

The reduction potential of the reaction is then given by

$$E_{cell} = -\frac{\Delta G_{rxn}^o}{nF} - E_{SHE} \quad (3)$$

We need not consider the free energy of solvation of the electron as their contribution cancels out when we consider the full reaction against experimentally measured values.²⁷

To decide on the best functional for the present study, we did a benchmarking study on the reduction potential of our substrates *trans*-anethole **1a** and *trans*- β -methylstyrene **1b** in MeCN solvent using a number of functionals. The results are given in Table S1, which shows that M06-2X functional gives the best agreement (smallest mean unsigned error) with the experimental redox potential values amongst 8 functionals tested. This is in agreement with a study of both experimental and computational electrochemical potentials for over 180 organic substrates where M06-2X functional gives an R^2 value of 0.97 for the correlation between the experimental and calculated redox potentials.²⁸ We used M06-2X for all subsequent DFT calculations.

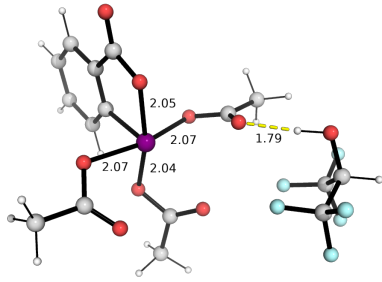
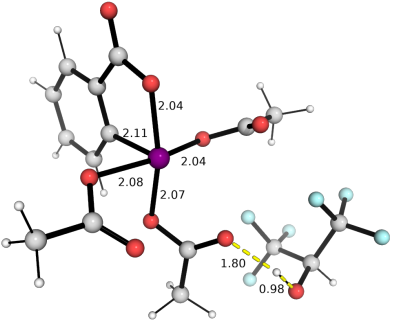
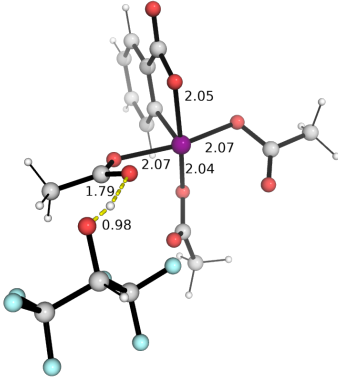
	Expt ^a	B3LYP	B3LYP-D3	B97D	CAM-B3LYP	M06-2X	revPBE	TPSS-D3	ω B97X-D
1a	1.484	1.184	1.183	0.975	1.289	1.388	1.162	1.006	1.203
1b	1.984	1.621	1.587	1.430	1.709	1.815	1.604	1.461	1.635

^a Values are taken from ref.²⁸ where potentials are reported against standard calomel electrode in MeCN solvent (1.24V for **1a** and 1.74V for **1b**). These values are converted to be relative to SHE using conversion constants (+0.244V) in ref.²⁹ and then reported herein. For computational studies, a value of $E_{SHE} = 4.28\text{V}$ in SMD model is used.^{26,27,30}

Table S1 Computed reduction potentials of *trans*-anethole **1a** and *trans*- β -methylstyrene **1b** in MeCN solvent using a variety of functionals. All values are in V.

2.1 Conformational considerations for Dess-Martin periodinane (DMP), hexafluoroisopropanol (HFIP) and DMP-HFIP complex

For Dess-Martin periodinane (DMP), the reported X-ray crystal structure³¹ was used as the initial guess for DFT geometry optimization. For the structure of HFIP, 3 possible conformers were known to exist: antiperiplanar, synclinal and gauche.^{32,33} These were separated optimised using DFT and the lowest energy conformer in the gas-phase, the antiperiplanar form, which agrees with experimental observations, is used. We explored the conformations of the DMP-HFIP complex by placing the HFIP molecule, in turn, near one of the 3 acetates, at a distance between the furthest O-atom on acetate and the H-atom on alcohol group of HFIP of $> 3\text{\AA}$ and subjecting the structures (both neutral and radical anionic) to DFT optimisation at M06-2X/GENECP(LANL2DZ for I and 6-31+G(d) for others) and then correct for solvent effect at SMD(solvent)-M06-2X/def2-TZVPP level of theory. We then compared the resultant energies of the conformers to establish the ones with lowest energy in either MeCN or HFIP solvent for the neutral and radical anionic species. All the conformers found in this way were shown in Fig. S1. The lowest energy conformers were used for the computation of redox potential of DMP-HFIP complex.

Neutral DMP-HFIP complex		
DMP-HFIP-c1-n	DMP-HFIP-c2-n	DMP-HFIP-c3-n
$\Delta\Delta G = 0.0$ (1.2)	0.7 (0.0)	2.2 (3.1)
		
Radical anionic DMP-HFIP complex		
DMP-HFIP-c1-ra	DMP-HFIP-c2-ra	DMP-HFIP-c3-ra
$\Delta\Delta G = 0.0$ (0.0)	3.4 (0.6)	4.6 (7.3)

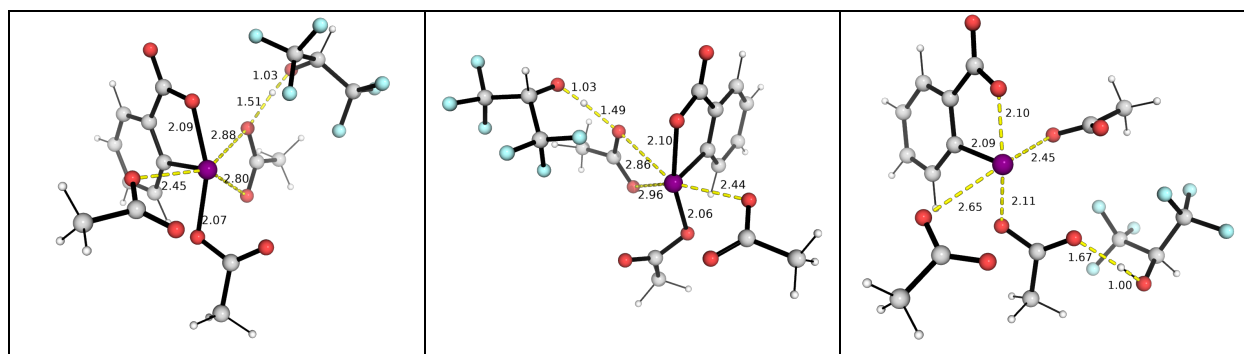
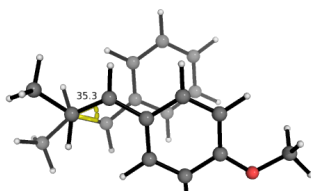
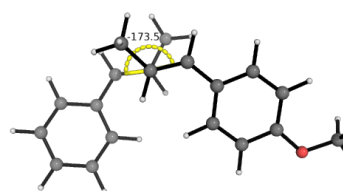
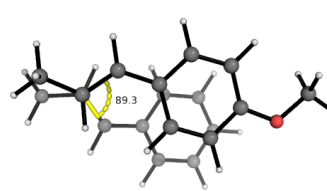


Fig. S1. Conformations of optimised DMP-HFIP complex. Relative Gibbs energies are given in kcal mol⁻¹. Values are for HFIP solvent with values for MeCN solvent given in brackets. The lowest energy conformer within each of the neutral and radical anionic species is taken as energy zero.

3. Reaction P1 (*trans*-anethole + *trans*- β -methylstyrene)

For complete conformational sampling of all the TSs involved in the first C–C bond formation, once a TS is found (for example **ts1** in Fig. S2), we rotate one of the reactant, say *t*-anethole along the forming C–C bond by 120° (since there are 3 groups on each carbon atom involved in the C–C bond formation), and carry out TS search. For the example of **ts1**, we were able to find **ts1-c2** and **ts1-c3** in this way. Similarly, **ts1'**, **ts1'-c2** and **ts1'-c3** are found for the *syn*-addition.

ts1	ts1-c2	ts1-c3
13.5 [‡] (18.2 [‡])	15.7 [‡] (18.4 [‡])	15.7 [‡] (21.2 [‡])
		
r = 2.09 Å	r = 2.15 Å	r = 2.04 Å
ts1-c4	ts2	ts1'
18.3 [‡] (21.4 [‡])	13.0 [‡] (16.2 [‡])	14.6 [‡] (17.6 [‡])

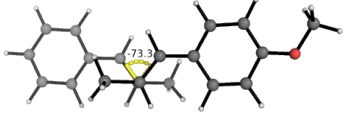
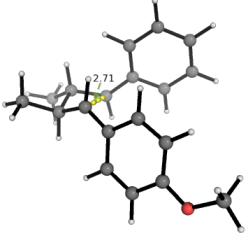
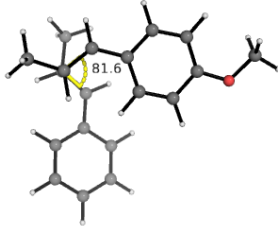
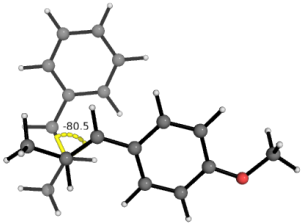
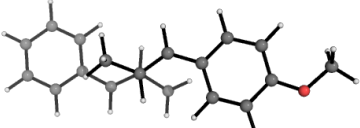
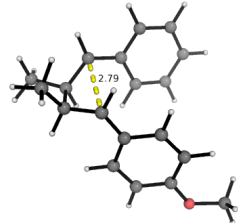
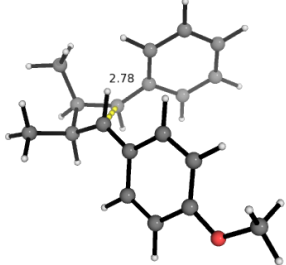
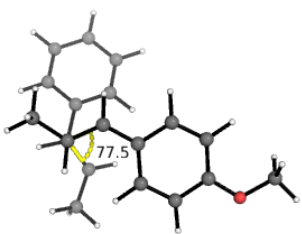
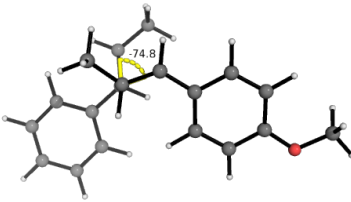
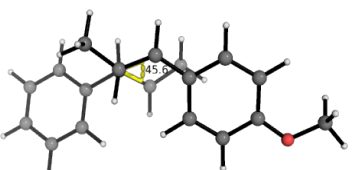
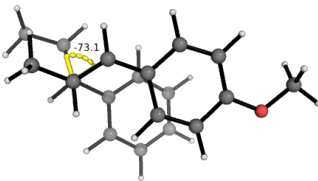
		
$r = 2.01 \text{ \AA}$	$r = 1.57 \text{ \AA}$	$r = 2.18 \text{ \AA}$
ts1'-c2	ts1'-c3	ts2'
14.6 [‡] (18.0 [‡])	17.6 [‡] (20.8 [‡])	12.3 [‡] (15.7 [‡])
		
$r = 2.10 \text{ \AA}$	$r = 2.12 \text{ \AA}$	$r = 1.59 \text{ \AA}$
ts2'-c2	ts1-g1	ts1-g1-c2
12.5 [‡] (16.3 [‡])	19.3 [‡] (22.8 [‡])	22.1 [‡] (24.8 [‡])
		
$r = 1.56 \text{ \AA}$	$r = 1.96 \text{ \AA}$	$r = 1.81 \text{ \AA}$
ts1-g2	ts1-g2-c2	
20.8 [‡] (24.4 [‡])	20.9 [‡] (25.6 [‡])	
		
$r = 1.93 \text{ \AA}$	$r = 1.82 \text{ \AA}$	

Fig. S2. Conformations of all TSs for the reaction between *trans*-anethole and *trans*- β -methylstyrene (P1). Distances of the first C–C bond formation (r) is given. Gibbs energies are given in kcal mol⁻¹. Values are for HFIP solvent with values for MeCN solvent given in brackets.

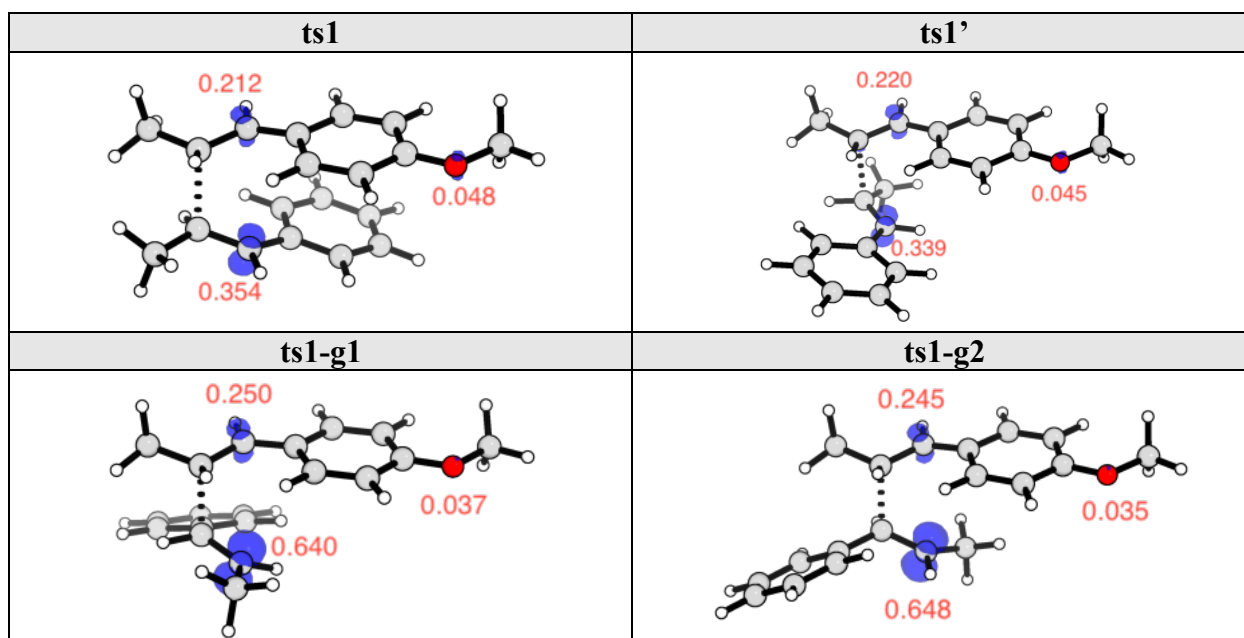


Fig. S3. Spin density plots (at an isovalue of 0.02 a.u.) and the Mulliken spin density values of radical cationic TSs in reaction P1.

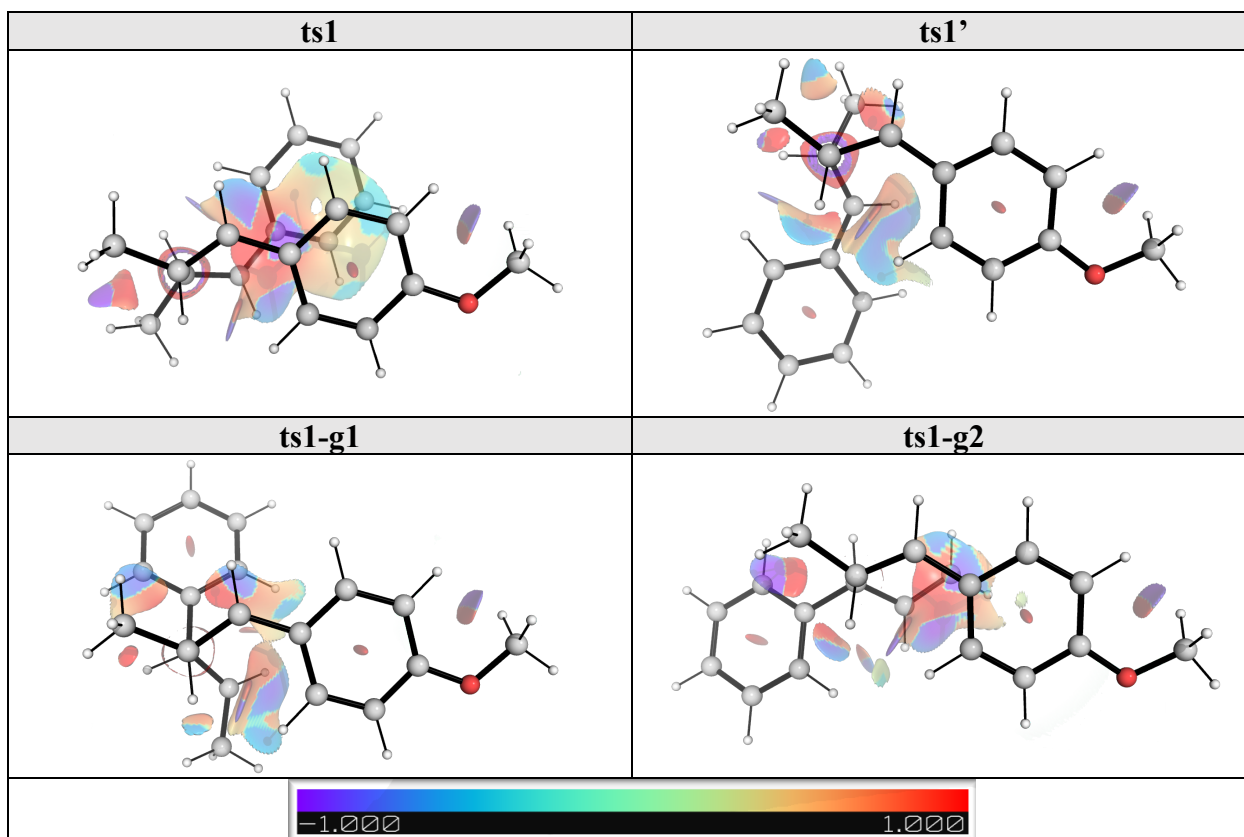


Fig. S4. NCI plots for head-to-head and head-to-tail first C–C bond formations TSs in reaction P1.

The distortion-interaction^{34,35}/activation strain (DI-AS) model^{35–38} was applied to understand the steric and electronic factors controlling the selectivity of cyclobutene formation. To further break down the electronic contributions and understand the contributions of the interaction energy in terms of nature of chemical bonds, we applied the energy decomposition analysis (EDA) to the TSs for the formation of cyclobutanes. EDA breaks down the interaction energy into repulsive exchange energy due to Pauli's principle, E_{Pauli} , the (semi-)classical electrostatic interaction energy between the charge densities of the fragments, E_{elec} , the orbital interaction energies between the fragments as the TS occurs, E_{orb} , and the dispersion energy between the fragments E_{disp} . Fig. S5 to Fig. S8 shows the individual DI-AS energy and the EDA analysis for key TSs in reaction P1.

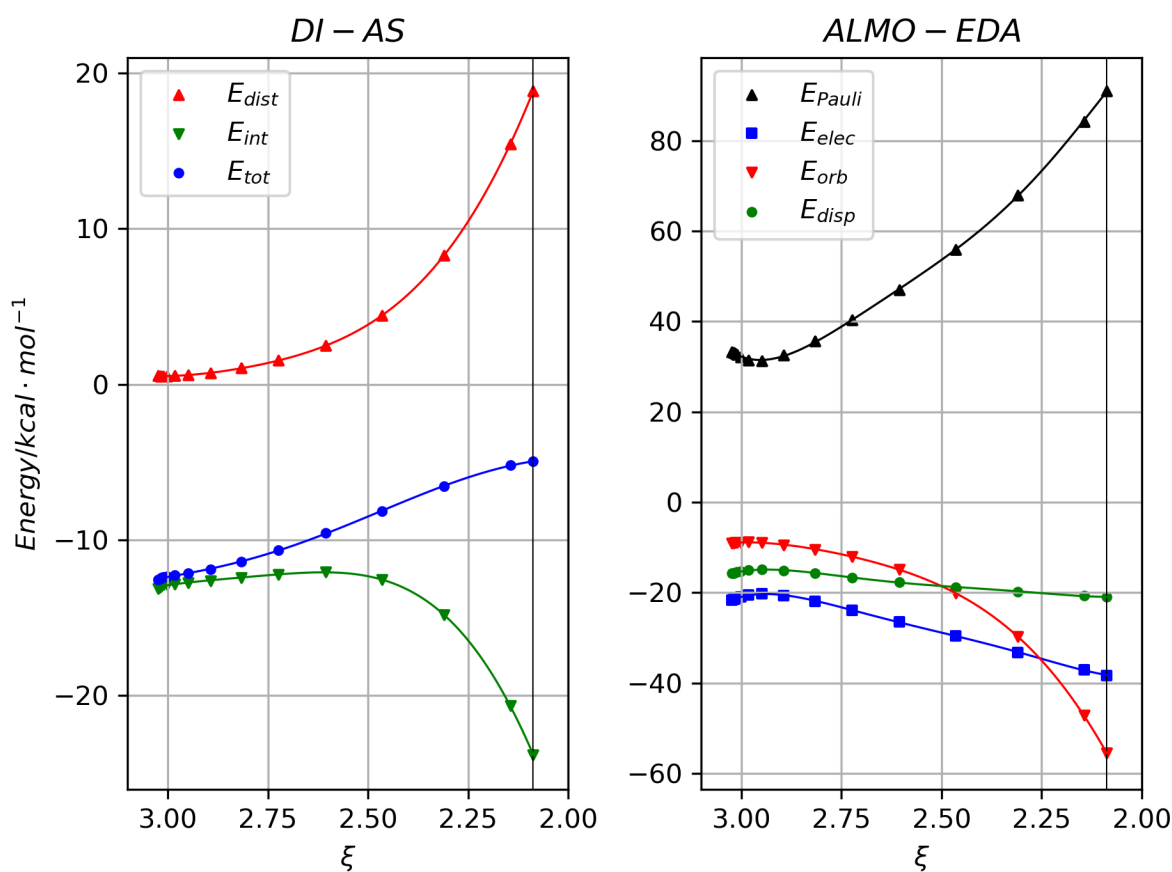


Fig. S5. Distortion interaction-action strain model (DI-AS) and absolutely-localized molecular orbitals energy decomposition analysis (ALMO-EDA) for **ts1** (*anti*-addition) in reaction P1.

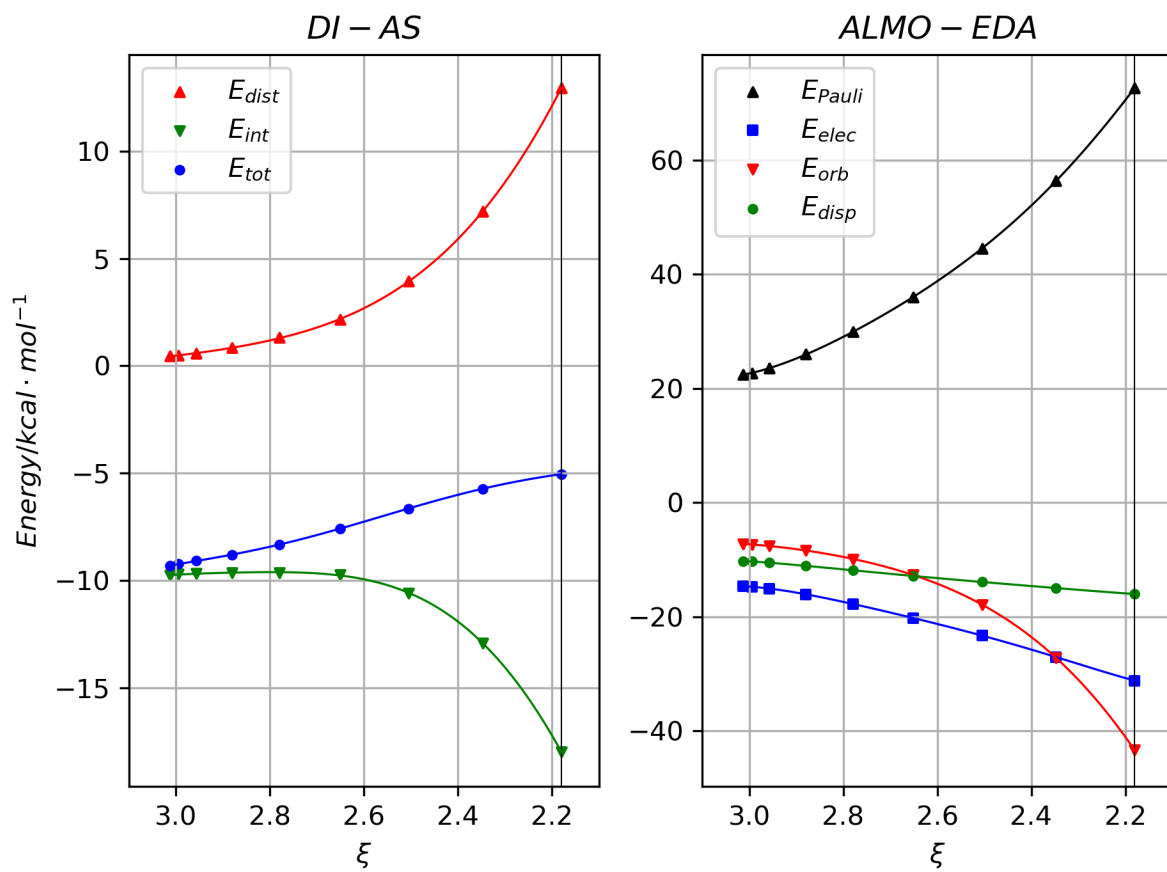


Fig. S6. Distortion interaction-action strain model (DI-AS) and absolutely-localized molecular orbitals energy decomposition analysis (ALMO-EDA) for **ts1'** (*syn*-addition) in reaction P1.

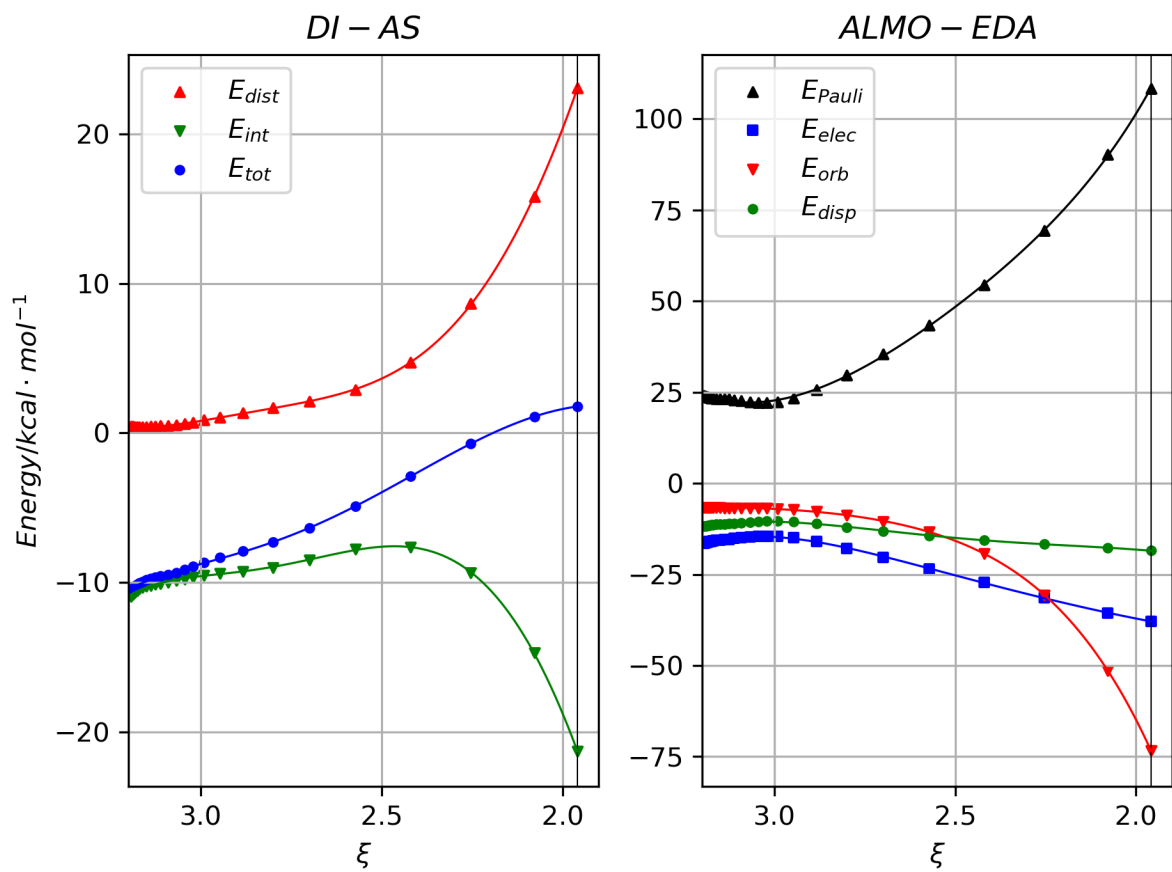


Fig. S7. Distortion interaction-action strain model (DI-AS) and absolutely-localized molecular orbitals energy decomposition analysis (ALMO-EDA) for **ts1-g1** in reaction P1.

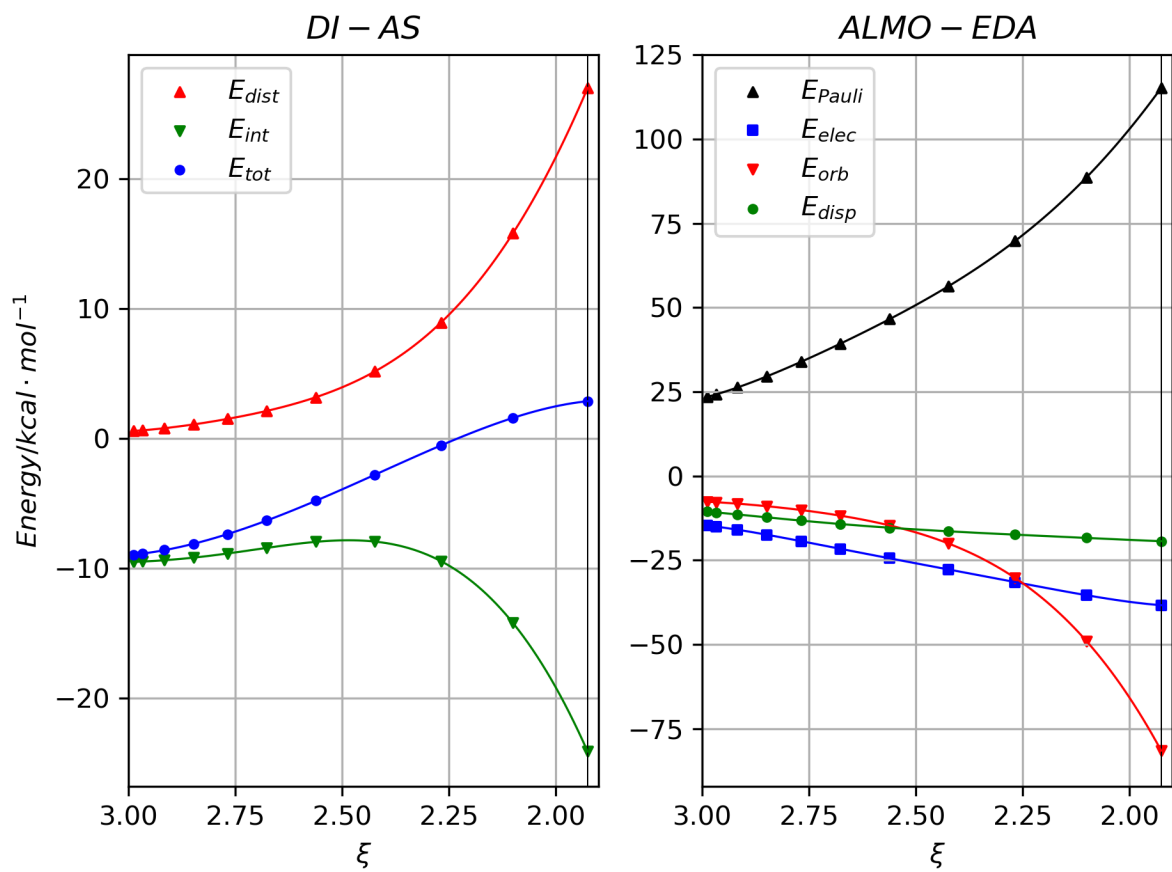


Fig. S8. Distortion interaction-action strain model (DI-AS) and absolutely-localized molecular orbitals energy decomposition analysis (ALMO-EDA) for **ts1-g2** in reaction P1.

In Fig. S9 to Fig. S11, we do a pairwise comparison (between the major product and the other products) of the individual contributions to the interaction energy governing the selectivity in the TSs in reaction P1. Legend for the plots follow those in Fig. 3 in the main text.

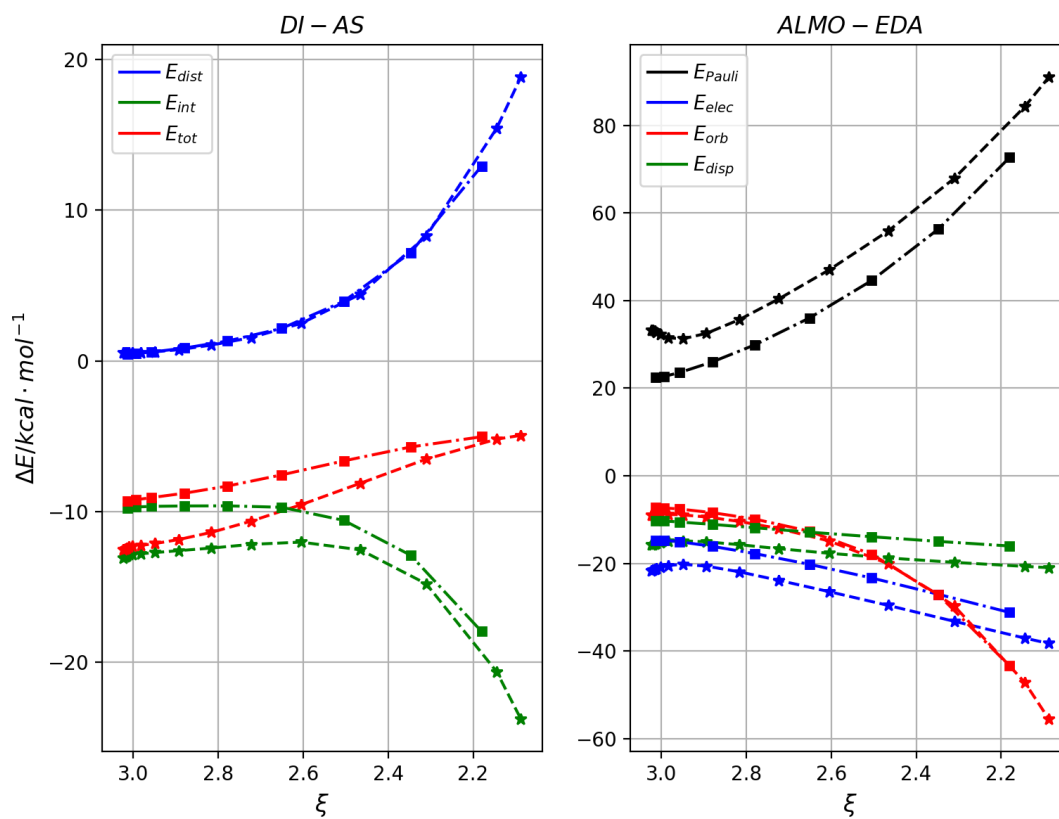


Fig. S9. Comparison of the distortion interaction-action strain model (DI-AS) and absolutely-localized molecular orbitals energy decomposition analysis (ALMO-EDA) for $ts1$ (star marker) and $ts1'$ (square marker) in reaction P1.

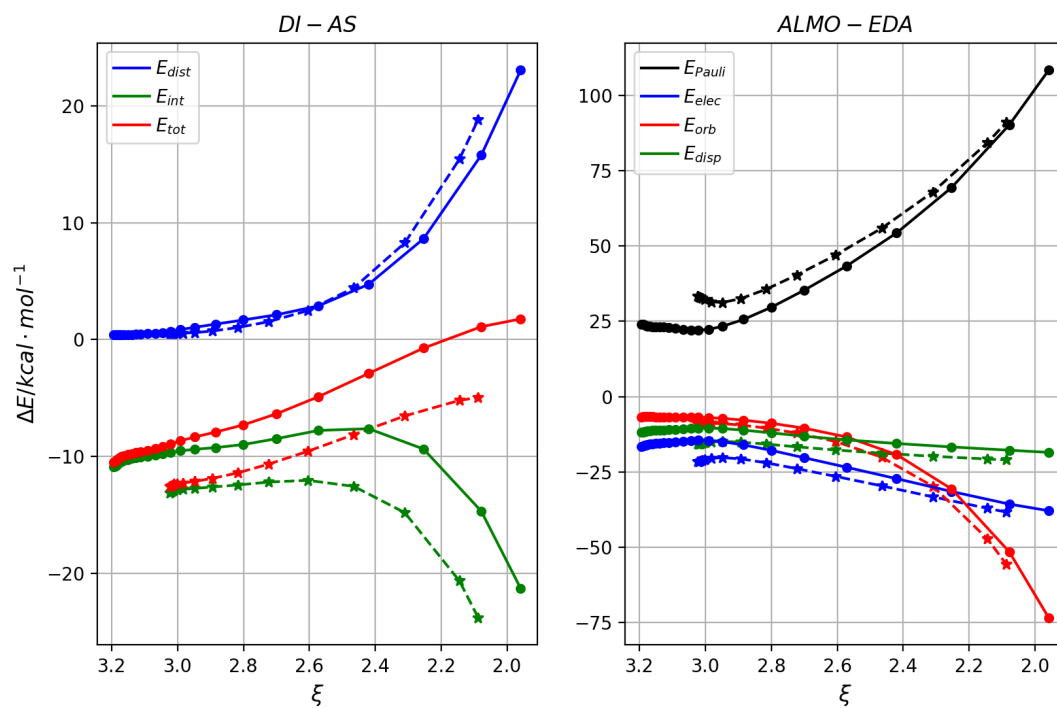


Fig. S10. Comparison of the distortion interaction-action strain model (DI-AS) and absolutely-localized molecular orbitals energy decomposition analysis (ALMO-EDA) for **ts1** (star marker) and **ts1-g1** (full circle marker) in reaction P1.

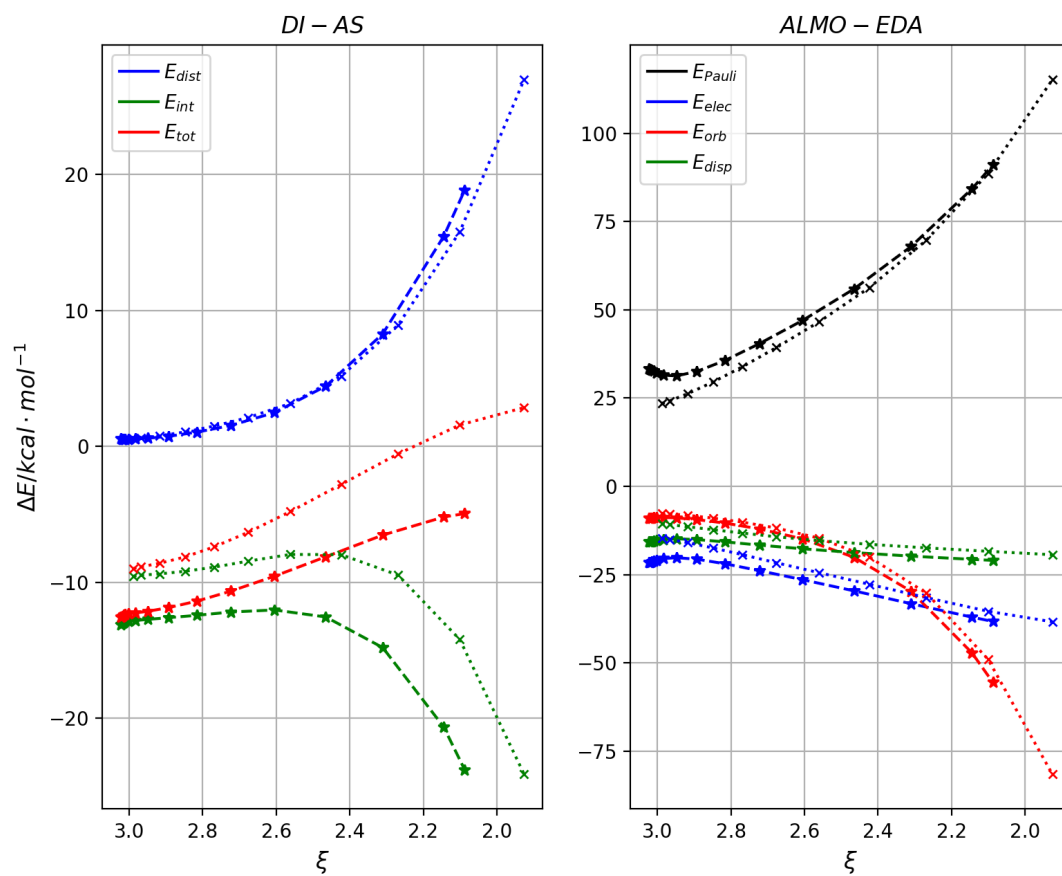
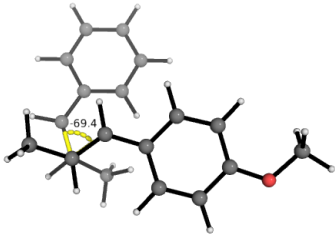
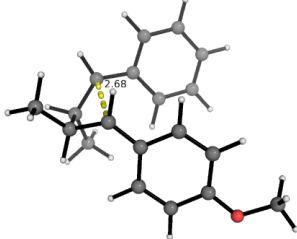
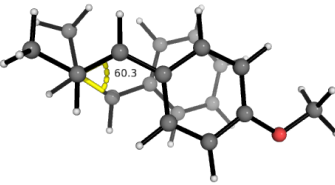
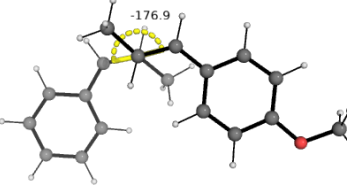
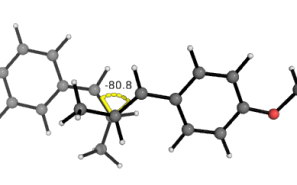
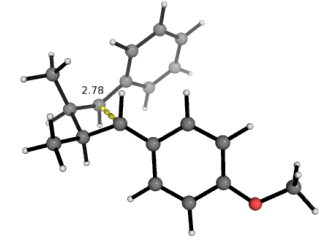
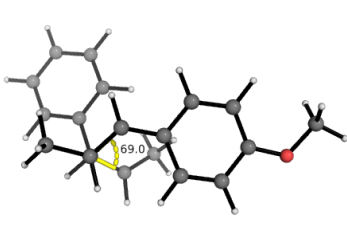
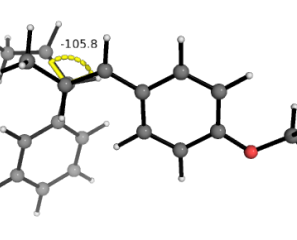


Fig. S11. Comparison of the distortion interaction-action strain model (DI-AS) and absolutely-localized molecular orbitals energy decomposition analysis (ALMO-EDA) for **ts1** (star marker) and **ts1-g2** (cross marker) in reaction P1.

4. Reaction P2 (*trans*-anethole + *cis*- β -methylstyrene)

Conformational sampling of all the TSs involved in the first C–C bond formation for this pathway were done in a similar fashion as described for reaction P1 in section 3.

ts6	ts6-c2	ts7
19.3 [‡] (22.7 [‡])	21.2 [‡] (24.6 [‡])	17.4 [‡] (21.1 [‡])
		
r = 2.09 Å	r = 2.12 Å	r = 1.58 Å
ts6'	ts6'-c2	ts6'-c2
16.1 [‡] (21.7 [‡])	20.1 [‡] (22.9 [‡])	21.1 [‡] (23.6 [‡])
		
r = 2.07 Å	r = 2.13 Å	r = 1.97 Å
ts7'	ts6-g1	ts6-g1-c2
17.4 [‡] (20.3 [‡])	21.3 [‡] (25.0 [‡])	26.5 [‡] (29.9 [‡])
		
r = 1.58 Å	r = 1.94 Å	r = 1.81 Å
ts6-g2	ts6-g2-c2	
22.6 [‡] (27.1 [‡])	23.6 [‡] (26.9 [‡])	

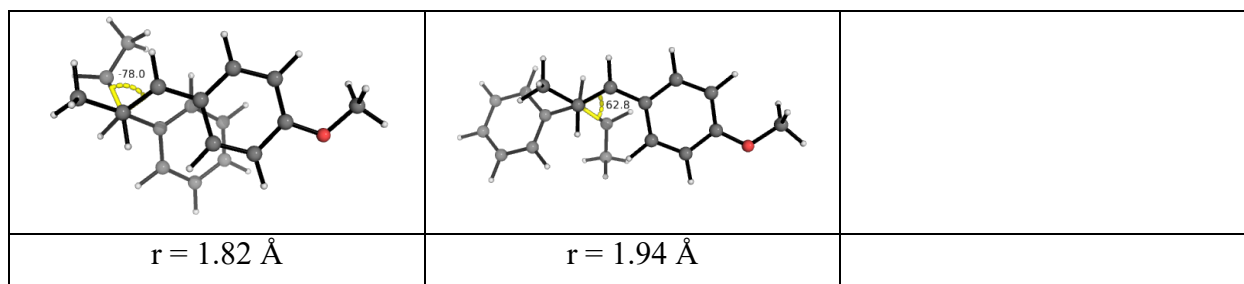


Fig. S12. Conformations of all TSs for the reaction between *trans*-anethole and *cis*- β -methylstyrene (P2). Distances of the first C–C bond formation (r) is given. Gibbs energies are given in kcal mol⁻¹. Values are for HFIP solvent with values for MeCN solvent given in brackets.

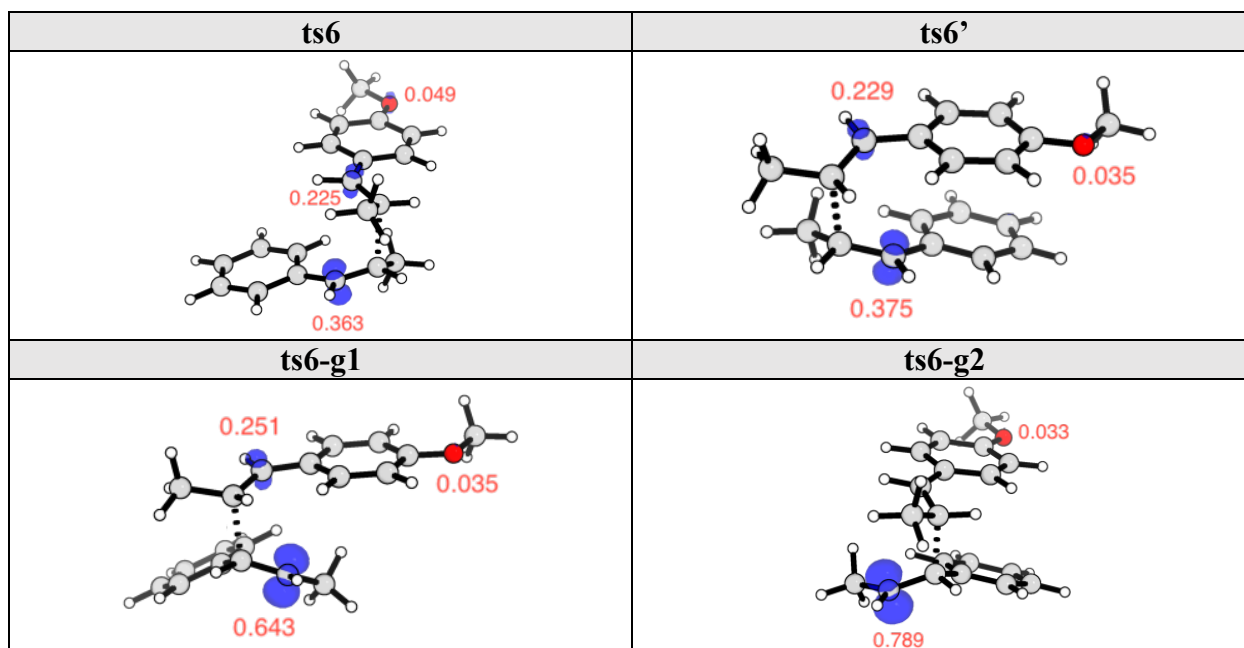


Fig. S13. Spin density plots (at an isovalue of 0.02 a.u.) and the Mulliken spin density values of radical cationic TSs for the reaction between *trans*-anethole and *cis*- β -methylstyrene.

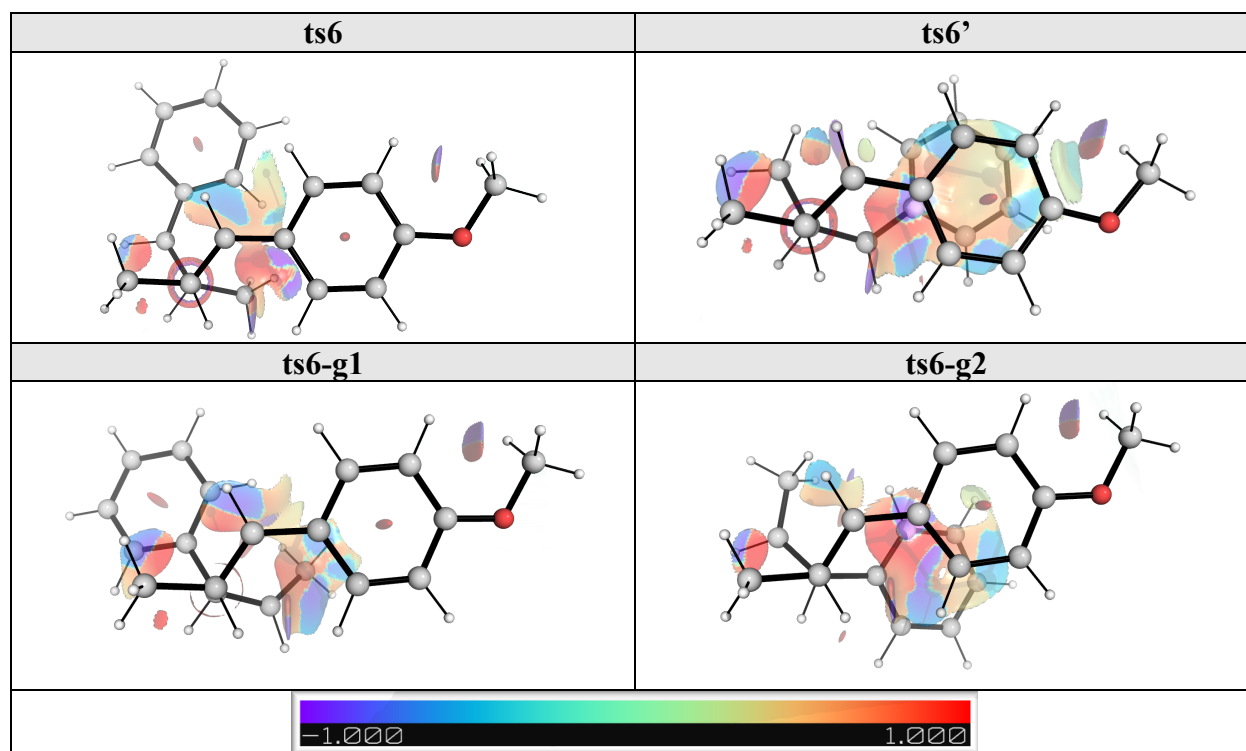


Fig. S14. NCI plots for head-to-head and head-to-tail first C–C bond formations TSs in reaction P2.

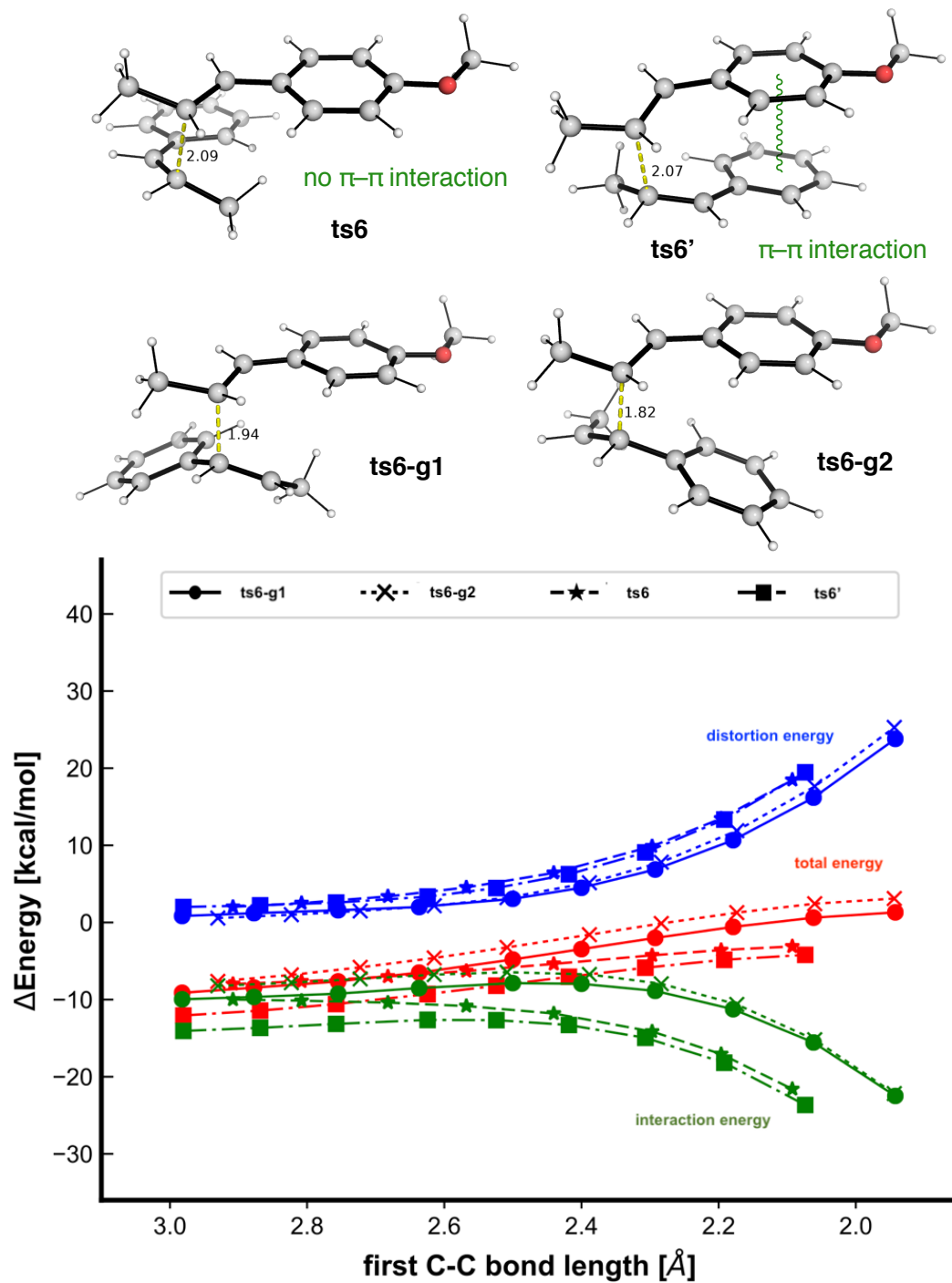


Fig. S15. The activation strain or distortion-interaction analyses applied to transition structures for both head-to-head (**ts6** and **ts6'**) and head-to-tail (**ts6-g1** and **ts6-g2**) first C-C bond formation TSs. All energies are calculated at UM062X/def2TZVPP//UM062X/6-31G(d) and used without any further corrections.

Similar DI-AS/EDA results for the key TSs are shown in Fig. S16 to Fig. S19.

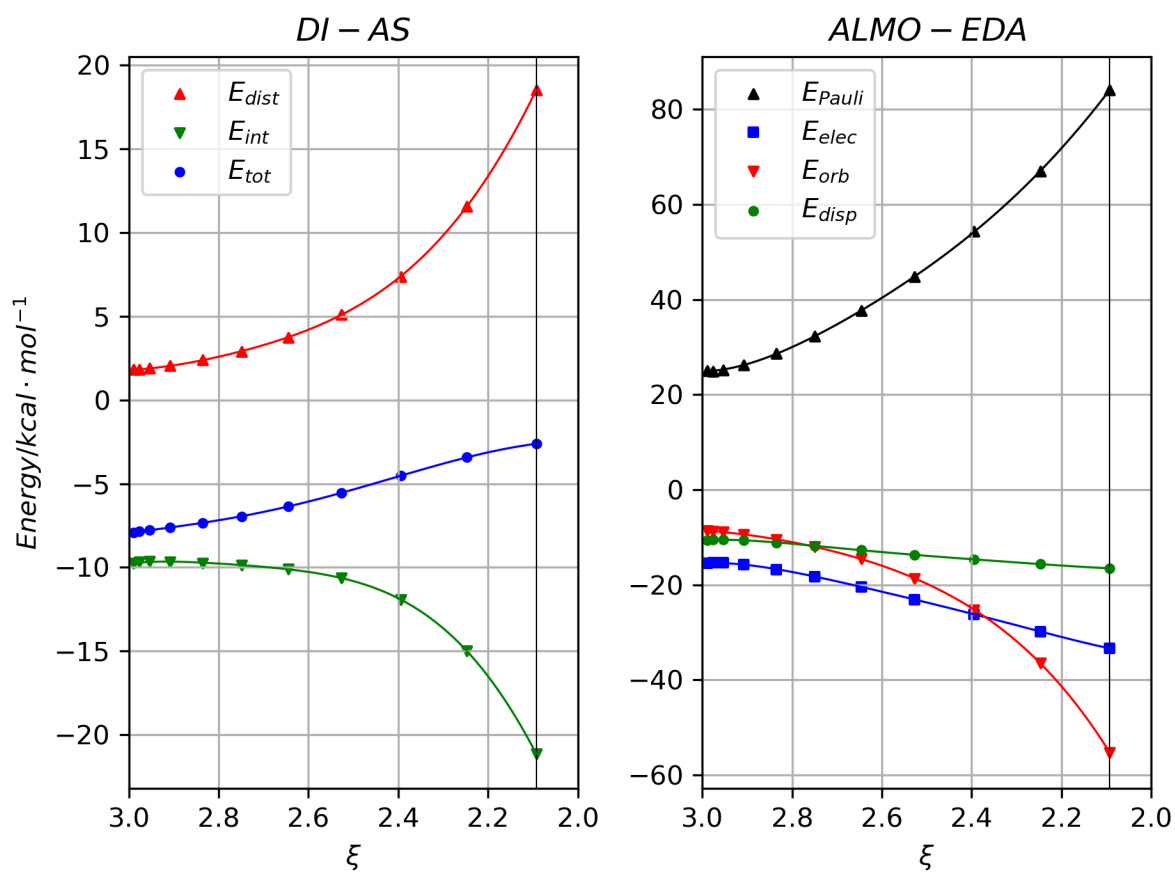


Fig. S16. Distortion interaction-action strain model (DI-AS) and absolutely-localized molecular orbitals energy decomposition analysis (ALMO-EDA) for **ts6** (*anti*-addition) in reaction P2.

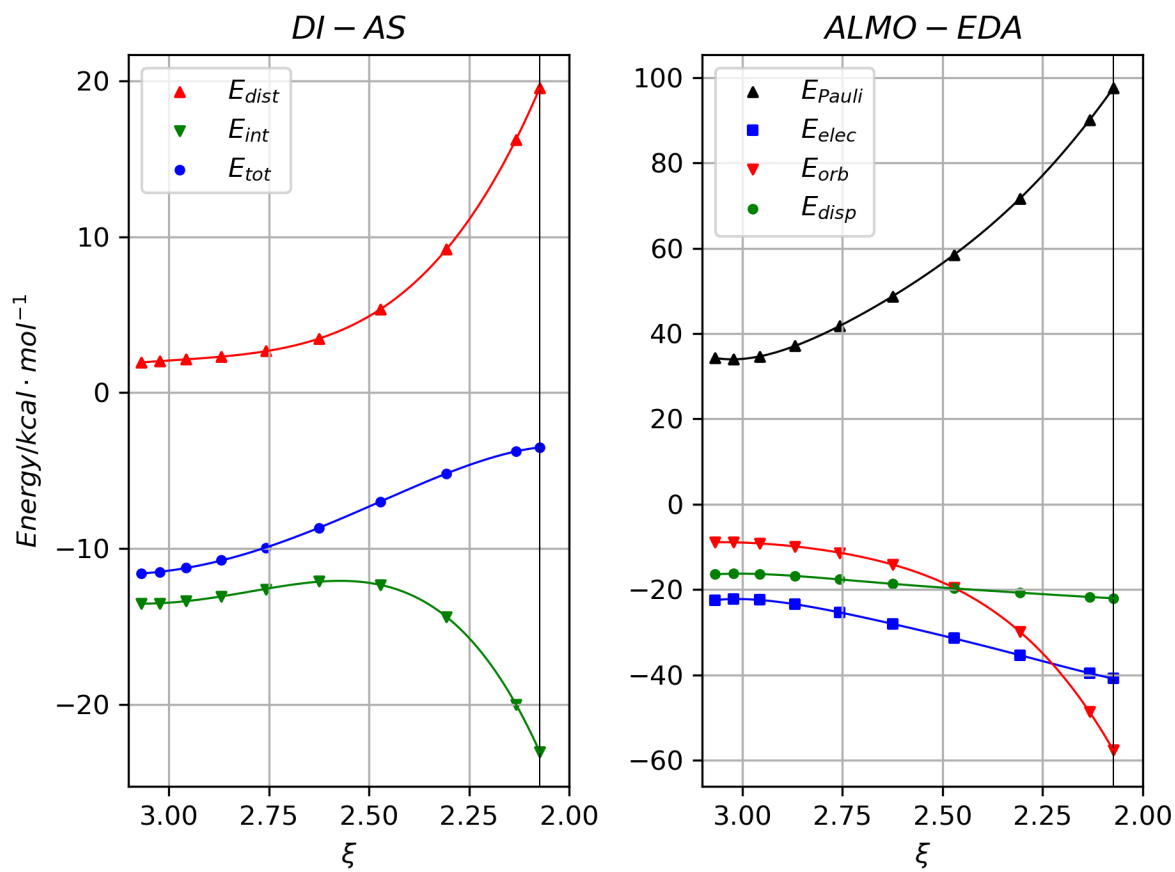


Fig. S17. Distortion interaction-action strain model (DI-AS) and absolutely-localized molecular orbitals energy decomposition analysis (ALMO-EDA) for **ts6'** (*syn*-addition) in reaction P2.

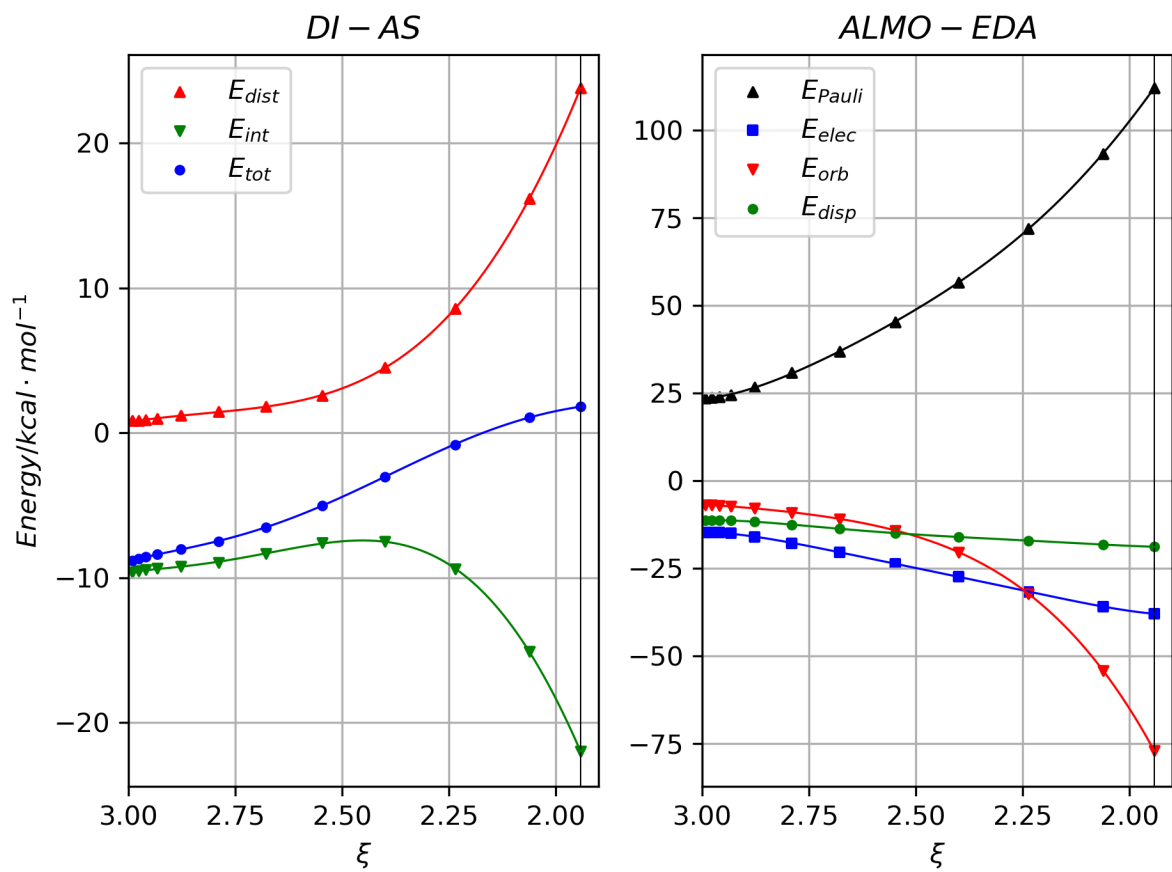


Fig. S18. Distortion interaction-action strain model (DI-AS) and absolutely-localized molecular orbitals energy decomposition analysis (ALMO-EDA) for **ts6-g1** in reaction P2.

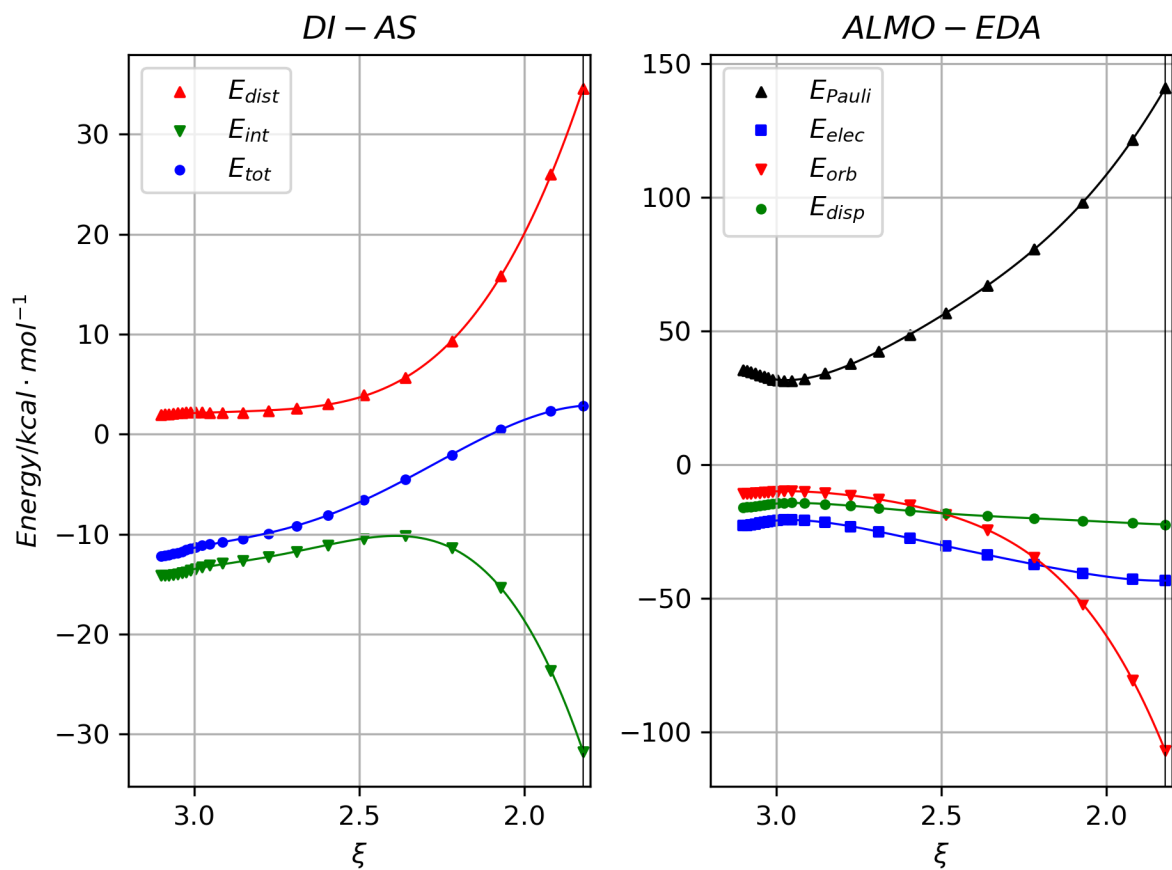


Fig. S19. Distortion interaction-action strain model (DI-AS) and absolutely-localized molecular orbitals energy decomposition analysis (ALMO-EDA) for **ts6-g2** in reaction P2.

The comparison between the major product and the other products of the individual contributions to the interaction energy governing the selectivity in the TSs in reaction P2 is shown in Fig. S20 to Fig. S22. Legend for the plots follow those in Fig. S15.

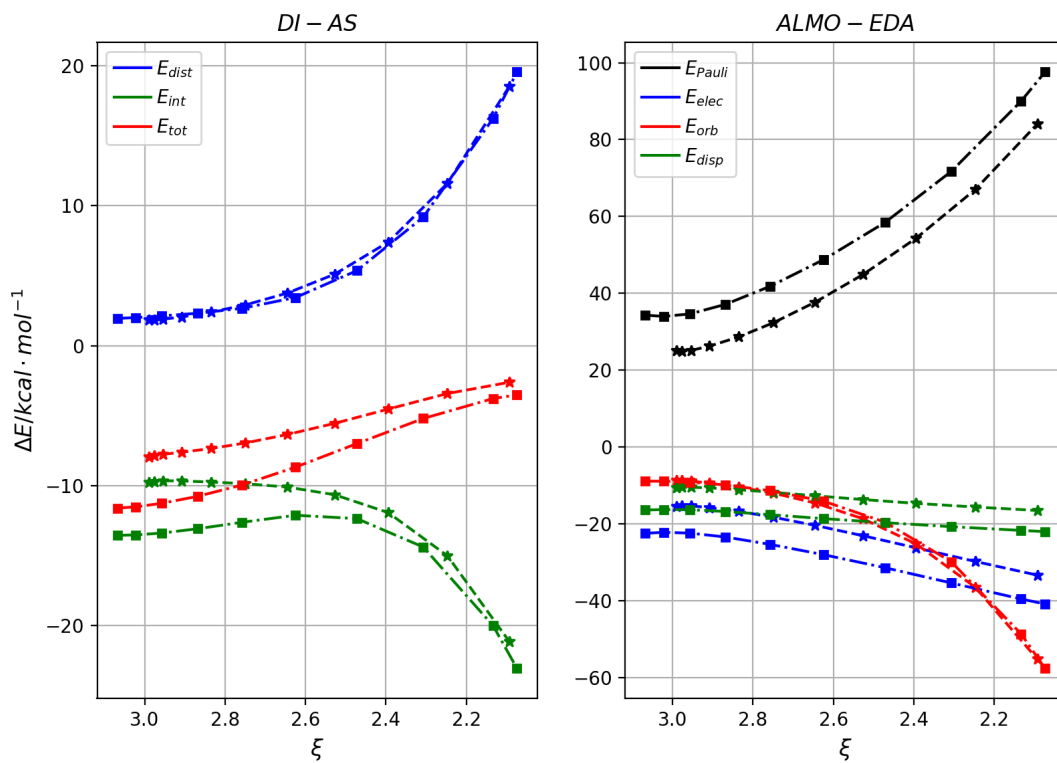


Fig. S20. Comparison of the distortion interaction-action strain model (DI-AS) and absolutely-localized molecular orbitals energy decomposition analysis (ALMO-EDA) for **ts6'** (square marker) and **ts6*** (star marker) in reaction P2.

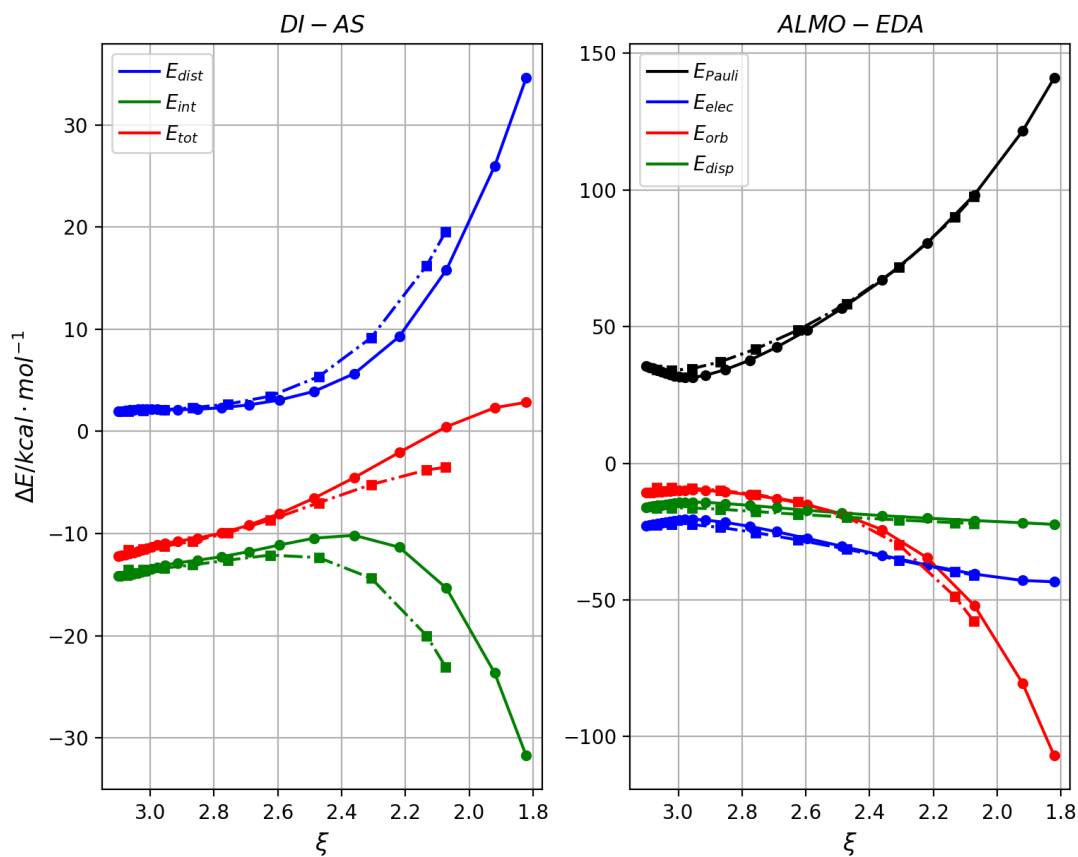


Fig. S21. Comparison of the distortion interaction-action strain model (DI-AS) and absolutely-localized molecular orbitals energy decomposition analysis (ALMO-EDA) for **ts6*** (square marker) and **ts6-g1** (full circle marker) in reaction P2. The dominant difference in the interaction comes from the charge transfer term (RHS) which is $\sim 5 \text{ kcal mol}^{-1}$ at around 2.07 \AA (note the large y-axis scale that makes this less obvious).

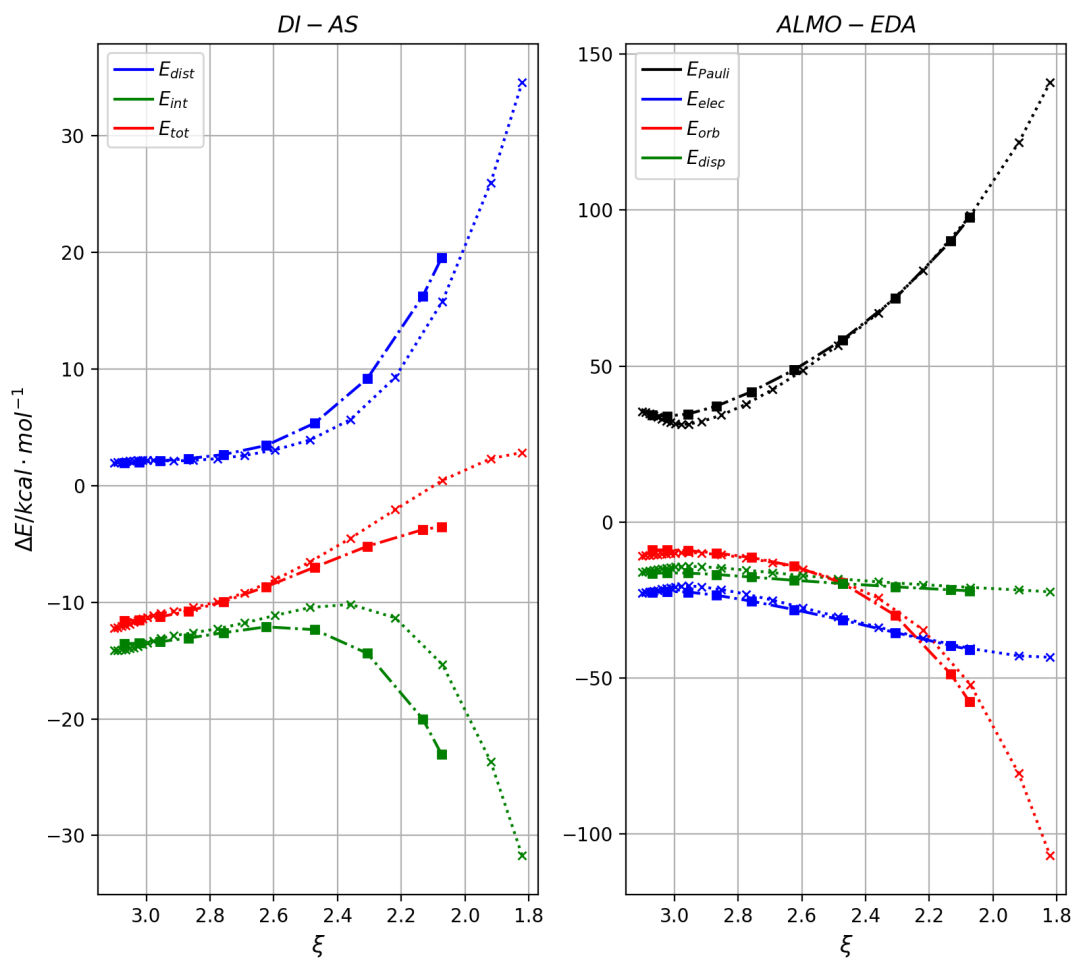
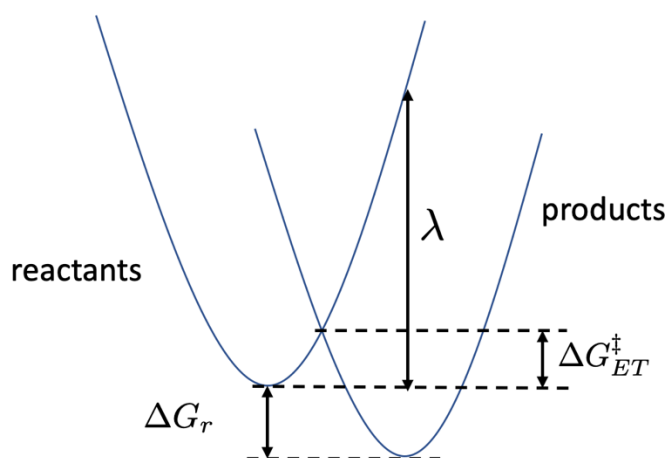


Fig. S22. Comparison of the distortion interaction-action strain model (DI-AS) and absolutely-localized molecular orbitals energy decomposition analysis (ALMO-EDA) for **ts6'** (square marker) and **ts6-g2** (cross marker) in reaction P2. The dominant difference in the interaction comes from the charge transfer term (RHS) which is $\sim 5.5 \text{ kcal mol}^{-1}$ at around 2.07 \AA (note the large y-axis scale that makes this less obvious).

5. Estimate of electron transfer barrier

The Marcus-Hush³⁹⁻⁴² theory is used to relate quantitatively the rate of electron transfer (k_{ET}) to the Gibbs energy of a reaction (ΔG_r). In this framework, molecules involved in the electron transfer (ET) are treated as spheres and the solvent is treated as a continuum. Parabolic energy curves are used to represent the states of reactants and products. It is further assumed that the two parabolas have the same curvature. Within the diabatic representation (where the coupling between the two potential energy surfaces is due to electronic terms), the TS for the electron transfer (ET) occurs at where the two parabolas cross (Scheme S2).

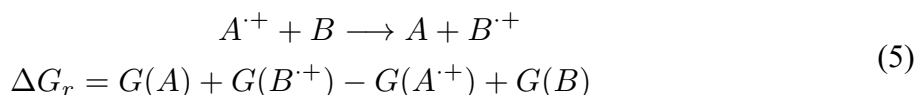


Scheme S2. Schematic representation of Marcus-Hush theory using parabolic Gibbs energy curves of the reactants and products.

With these, the activation energy of the ET, ΔG_{ET}^\ddagger , is given by

$$\Delta G_{ET}^\ddagger = \frac{\lambda}{4} \left(1 + \frac{\Delta G_r}{\lambda} \right) \quad (4)$$

where ΔG_r is the free energy change of the reaction, in our case for the reduction of radical cation ($A^{\bullet+}$) by a neutral species (B), this is given by



λ is the reorganisation energy, which is defined as the energy required to distort the reactant molecules and the surrounding solvent shell to that of the product in its equilibrium (Scheme S2).

The rate of electron transfer, k_{ET} , is then related to the activation energy of the ET, ΔG_{ET}^\ddagger , via an Arrhenius-like expression:

$$k_{ET} = Ae^{-\Delta G^\ddagger/RT} \quad (6)$$

The reorganisation energy is composed of two parts, the internal reorganisation energy, λ_i , and external polarisation, λ_o , i.e., $\lambda = \lambda_i + \lambda_o$. The former term λ_i describes the energy associated with geometry changes when going from the reactant to the product state; the latter term λ_o describes the energy change due to the polarisation/reorganisation in the surrounding (solvent) molecules due to the ET process.

In our estimation of the ET barriers, we assume that the geometry change upon electron transfer is small such that we can ignore the internal reorganisation energy ($\lambda_i = 0$). Thus, $\lambda = \lambda_o$. Using Marcus equation, the solvent reorganisation energy is given by³⁹⁻⁴²

$$\begin{aligned} \lambda_o &= (\Delta e)^2 \cdot \left[\frac{1}{2a_1} + \frac{1}{2a_2} - \frac{1}{R} \right] \cdot \left[\frac{1}{\epsilon_{op}} - \frac{1}{\epsilon} \right] \\ &= (322 \text{ kcal mol}^{-1}) \left[\frac{1}{2a_1} + \frac{1}{2a_2} - \frac{1}{R} \right] \cdot \left[\frac{1}{\epsilon_{op}} - \frac{1}{\epsilon} \right] \end{aligned} \quad (7)$$

where Δe is the amount of charge transferred, a_1 and a_2 are the radii of the molecules involved (A and B in Equation 5), R is the distance between their centres, ϵ_{op} is the optical/dynamic dielectric constant ($\epsilon_{op} = 1.625625$) and ϵ is the static dielectric constant of the solvent ($\epsilon = 16.7$) (see values of HFIP solvent in the Computational Methods section). Hence, by calculating the molecular radii of the molecules (using *Gaussian* “volume” keyword and the recommended a_0 value) involved in an electron transfer process, we are able to estimate the barrier of such a process using the Marcus-Hush theory outlined above (Tables S2–4).

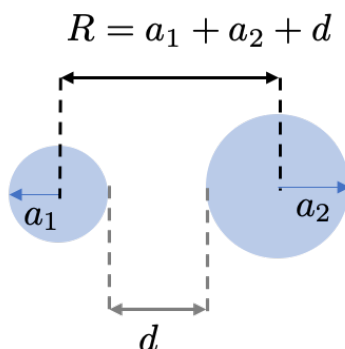
structure	<i>t</i> -anethole	int3	int3'	int8	int8'
Recommended $a_0/\text{\AA}$	4.69	4.95	5.40	5.39	5.12

Table S2. Computed recommended radii of structures involved in the electron transfer step in the reduction of radical cationic cyclobutyl ring to the neutral cyclobutyl ring by neutral *trans*-anethole.

The rate of electron transfer decreases exponentially with increasing separation between the species involved in the transfer due to the Arrhenius-like dependence of the rate equation on the barrier of ET (Eq. (6)). In Eq. (7), R is the distance between the centres of the two species. We investigated the dependence of the activation barrier of ET on the separation of molecules, d . The distance between two molecular centres R and the separation of the molecules d are related via

$$R = a_1 + a_2 + d \quad (8)$$

where a_1 and a_2 are the radii of the molecules involved (Scheme S3).



Scheme S3. Relation between the intermolecular separation d and the separation between two centres R that is used in Eq. (7).

Tables S3 and S4 are the computed values of λ and ΔG_{ET}^\ddagger in HFIP and in MeCN solvent, respectively. The corresponding plots showing the dependence of ΔG_{ET}^\ddagger on the intermolecular separation d is given in Fig. S23 and S24 respectively. Using an average intermolecular separation of 3.0 Å (c.f. intermolecular separation of 3.1 Å in liquid water), we estimate that the barriers for ET in HFIP solvent is on the order of 1–3 kcal mol⁻¹, whereas that in MeCN is on the order of 0–2 kcal mol⁻¹.

Separation	int3		int3'		Int8		Int8'	
	$\lambda / kcal$ mol^{-1}	$\Delta G_{ET}^\ddagger /$ $kcal$ mol^{-1}	$\lambda / kcal$ mol^{-1}	$\Delta G_{ET}^\ddagger /$ $kcal$ mol^{-1}	$\lambda / kcal$ mol^{-1}	$\Delta G_r /$ $kcal$ mol^{-1}	$\lambda / kcal$ mol^{-1}	$\Delta G_{ET}^\ddagger /$ $kcal$ mol^{-1}
0.00	18.6	1.6	17.9	1.6	17.9	0.4	18.3	1.1
0.25	19.0	1.8	18.3	1.7	18.3	0.5	18.7	1.3
0.50	19.5	1.9	18.7	1.8	18.7	0.6	19.2	1.4
0.75	19.9	2.0	19.1	1.9	19.1	0.7	19.6	1.5
1.00	20.3	2.1	19.5	2.0	19.5	0.8	20.0	1.6
1.25	20.7	2.2	19.8	2.1	19.9	0.9	20.4	1.7

1.50	21.1	2.3	20.2	2.1	20.2	1.0	20.7	1.8
1.75	21.4	2.4	20.5	2.2	20.5	1.1	21.1	1.8
2.00	21.8	2.4	20.8	2.3	20.8	1.2	21.4	1.9
2.25	22.1	2.5	21.1	2.4	21.1	1.2	21.7	2.0
2.50	22.4	2.6	21.4	2.5	21.4	1.3	22.0	2.1
2.75	22.7	2.7	21.7	2.5	21.7	1.4	22.3	2.1
3.00	23.0	2.7	22.0	2.6	22.0	1.4	22.6	2.2
3.25	23.3	2.8	22.2	2.7	22.2	1.5	22.8	2.3
3.50	23.5	2.9	22.5	2.7	22.5	1.6	23.1	2.3
3.75	23.8	2.9	22.7	2.8	22.7	1.6	23.3	2.4
4.00	24.0	3.0	22.9	2.8	22.9	1.7	23.6	2.5
4.25	24.2	3.1	23.1	2.9	23.2	1.7	23.8	2.5
4.50	24.5	3.1	23.4	2.9	23.4	1.8	24.0	2.6
4.75	24.7	3.2	23.6	3.0	23.6	1.8	24.2	2.6
5.00	24.9	3.2	23.8	3.0	23.8	1.9	24.4	2.7
5.25	25.1	3.3	24.0	3.1	24.0	1.9	24.6	2.7
5.50	25.3	3.3	24.1	3.1	24.2	2.0	24.8	2.8
5.75	25.5	3.4	24.3	3.2	24.4	2.0	25.0	2.8
6.00	25.7	3.4	24.5	3.2	24.5	2.1	25.2	2.9

Table S3. Computed solvent reorganisation energy λ and electron transfer barriers ΔG_{ET}^\ddagger for the reduction of radical cationic cyclobutyl rings to their neutral form by *t*-anethole in HFIP solvent. Optical dielectric constant ($\epsilon_{op} = 1.625625$) and static dielectric constant ($\epsilon = 16.7$) of the solvent HFIP were used in Eq. (7). $a_1 = 4.69$ Å is the radius of *t*-anethole; a_2 is the radius of radical cationic cyclobutyl ring ($a_2(\mathbf{int3}) = 4.95$ Å; $a_2(\mathbf{int3}') = 5.40$ Å; $a_2(\mathbf{int8}) = 5.39$ Å; $a_2(\mathbf{int8}') = 5.12$ Å as in Table S2). $R = a_1 + a_1 + d$ is the total separation between the centres of the species involved in ET (Scheme S3).

Separation	int3		int3'		Int8		Int8'	
$d/\text{\AA}$	$\lambda / \text{kcal mol}^{-1}$	$\Delta G_{ET}^{\ddagger} / \text{kcal mol}^{-1}$	$\lambda / \text{kcal mol}^{-1}$	$\Delta G_{ET}^{\ddagger} / \text{kcal mol}^{-1}$	$\lambda / \text{kcal mol}^{-1}$	$\Delta G_r / \text{kcal mol}^{-1}$	$\lambda / \text{kcal mol}^{-1}$	$\Delta G_{ET}^{\ddagger} / \text{kcal mol}^{-1}$
0.00	17.8	0.6	17.2	0.3	17.2	-0.8	17.6	0.0
0.25	18.3	0.7	17.6	0.4	17.6	-0.7	18.0	0.1
0.50	18.7	0.8	18.0	0.5	18.0	-0.6	18.4	0.2
0.75	19.1	0.9	18.4	0.6	18.4	-0.5	18.8	0.3
1.00	19.5	1.0	18.7	0.7	18.7	-0.4	19.2	0.4
1.25	19.9	1.1	19.0	0.8	19.1	-0.3	19.5	0.5
1.50	20.2	1.2	19.4	0.9	19.4	-0.3	19.9	0.6
1.75	20.6	1.3	19.7	0.9	19.7	-0.2	20.2	0.7
2.00	20.9	1.3	20.0	1.0	20.0	-0.1	20.5	0.7
2.25	21.2	1.4	20.3	1.1	20.3	0.0	20.8	0.8
2.50	21.5	1.5	20.6	1.2	20.6	0.0	21.1	0.9
2.75	21.8	1.6	20.8	1.2	20.8	0.1	21.4	0.9
3.00	22.1	1.6	21.1	1.3	21.1	0.2	21.7	1.0
3.25	22.3	1.7	21.3	1.4	21.3	0.2	21.9	1.1
3.50	22.6	1.8	21.6	1.4	21.6	0.3	22.2	1.1
3.75	22.8	1.8	21.8	1.5	21.8	0.4	22.4	1.2
4.00	23.0	1.9	22.0	1.5	22.0	0.4	22.6	1.3
4.25	23.3	1.9	22.2	1.6	22.2	0.5	22.8	1.3
4.50	23.5	2.0	22.4	1.6	22.4	0.5	23.1	1.4

4.75	23.7	2.1	22.6	1.7	22.6	0.6	23.3	1.4
5.00	23.9	2.1	22.8	1.7	22.8	0.6	23.5	1.5
5.25	24.1	2.2	23.0	1.8	23.0	0.7	23.7	1.5
5.50	24.3	2.2	23.2	1.8	23.2	0.7	23.8	1.6
5.75	24.5	2.2	23.3	1.9	23.4	0.7	24.0	1.6
6.00	24.7	2.3	23.5	1.9	23.5	0.8	24.2	1.6

Table S4. Computed solvent reorganisation energy λ and electron transfer barriers ΔG_{ET}^\ddagger for the reduction of radical cationic cyclobutyl rings to their neutral form by *t*-anethole in MeCN solvent. Optical dielectric constant, which is the square of the refractive index of acetonitrile 1.33934^{43} ($\epsilon_{op} = 1.79$) and static dielectric constant ($\epsilon = 38.8$)⁴³ of the solvent MeCN were used in Eq. (7). $a_1 = 4.69 \text{ \AA}$ is the radius of *t*-anethole; a_2 is the radius of radical cationic cyclobutyl ring ($a_2(\text{int3}) = 4.95 \text{ \AA}$; $a_2(\text{int3}') = 5.40 \text{ \AA}$; $a_2(\text{int8}) = 5.39 \text{ \AA}$; $a_2(\text{int8}') = 5.12 \text{ \AA}$ as in Table S2). $R = a_1 + a_2 + d$ is the total separation between the centres of the species involved in ET (Scheme S3).

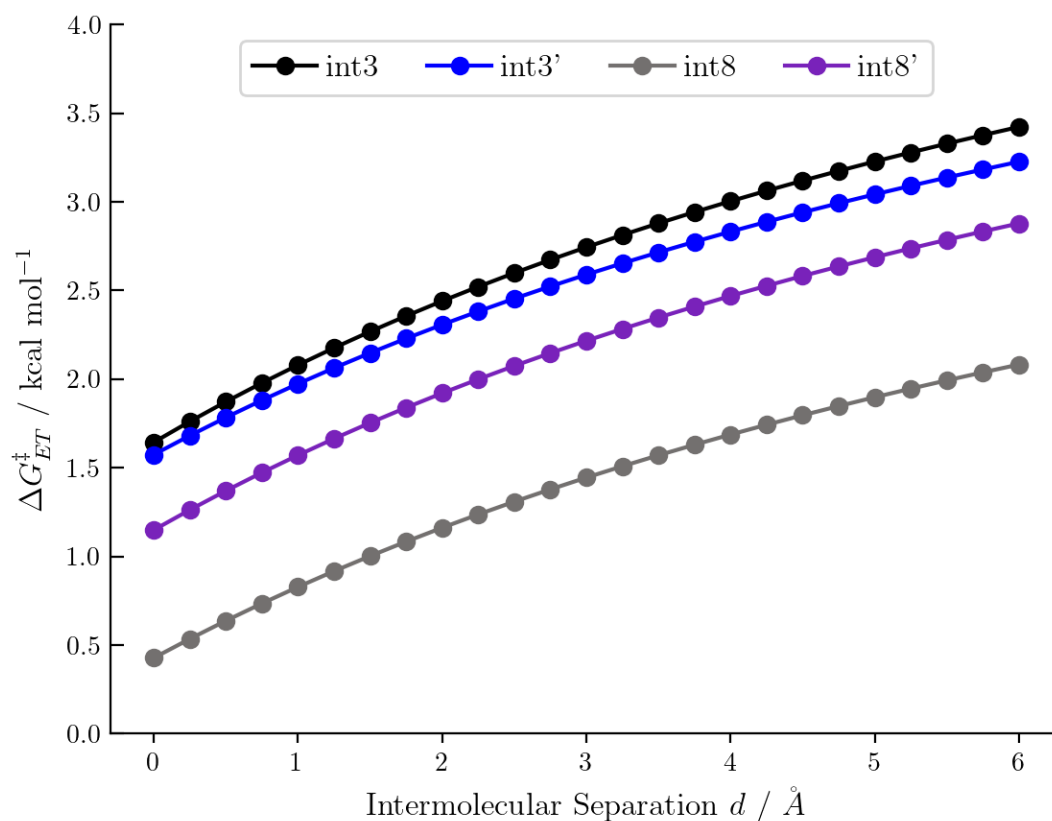


Fig. S23. Computed electron transfer barriers ΔG_{ET}^\ddagger as a function of intermolecular separation d in HFIP solvent plotted using data from Table S3.

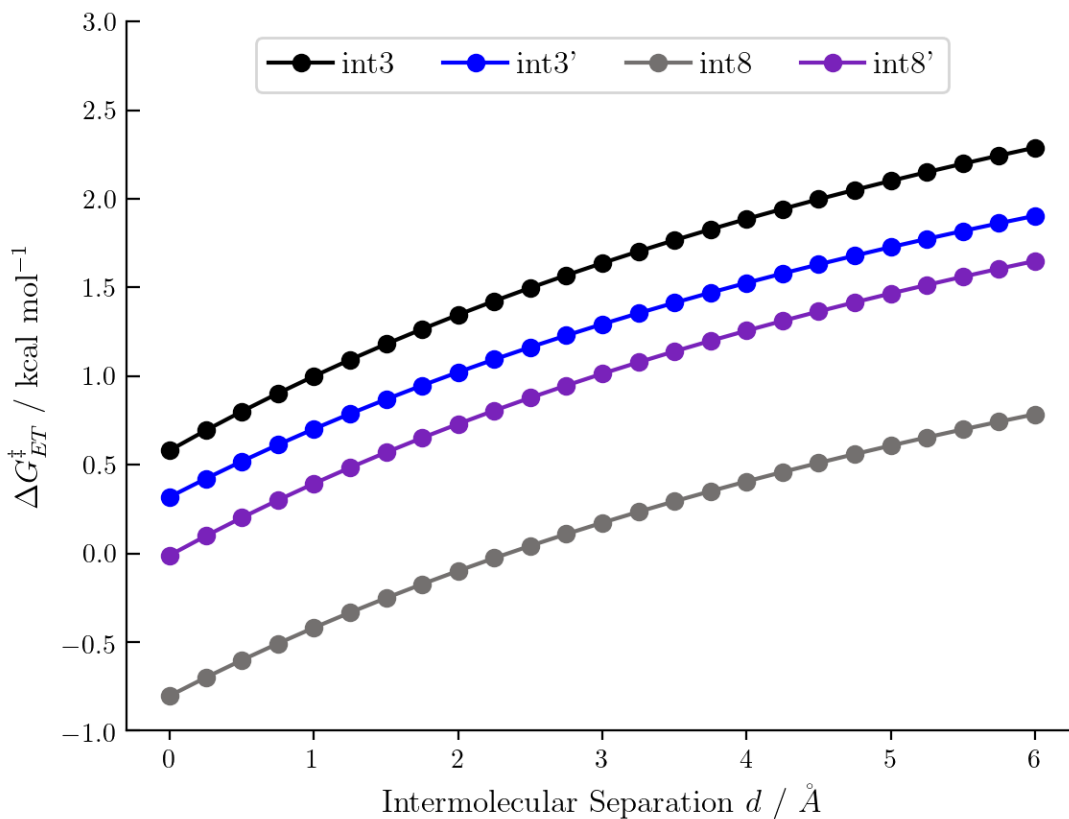


Fig. S24. Computed electron transfer barriers ΔG_{ET}^\ddagger as a function of intermolecular separation d in MeCN solvent plotted using data from Table S4.

Studies of both organic^{44–46} and inorganic^{47–49} systems in the gas phase revealed fast electron transfer rates close to diffusion limit. The reaction barriers are thus much smaller than that for the chemical transformations. It was also shown that the rate of electron transfer in gas phase is more than 10^4 times faster than in solvents.⁴⁹ We found that the ET barriers are very small (1–3 kcal mol⁻¹ in HFIP) for the reduction of radical cationic products to their neutral forms for the exergonic reactions. These calculations show that ET processes occur much faster than bond-forming events.

6. Absolute contribution to Gibbs energies

Structure	E/au	ZPE/au	H/au	qh-G/au	SP DFT (MeCN)	SP DFT (HFIP)
Starting materials:						
1a_n	-463.275335	0.196779	-463.06578	-463.113618	-463.47216	-463.45545
1a_rc	-463.009101	0.196496	-462.79962	-462.848486	-463.26901	-463.24939
1b_n	-348.797531	0.163449	-348.624	-348.665962	-348.94416	-348.93471
1b_rc	-348.508642	0.162615	-348.33574	-348.378687	-348.72508	-348.71327
2a_n	-463.272892	0.197361	-463.06308	-463.110068	-463.46919	-463.45309
2a_rc	-463.002658	0.197471	-462.79254	-462.840538	-463.26241	-463.24302
2b_n	-348.79484	0.16385	-348.6212	-348.662328	-348.9408965	-348.9320263
2b_rc	-348.50186	0.163047	-348.32873	-348.371138	-348.7182068	-348.7067152
Pathways for reaction P1:						
int1	-811.830601	0.361677	-811.4454	-811.51614	-812.22251	-812.2014
ts1	-811.8204	0.362952	-811.43567	-811.502488	-812.20993	-812.18829
ts1-c2	-811.819673	0.362972	-811.43472	-811.502623	-812.2087	-812.184
ts1-c3	-811.817037	0.363451	-811.43215	-811.498282	-812.20593	-812.18563
ts1-c4	-811.8155	0.36279	-811.43086	-811.4983	-812.2041	-812.1799
int2	-811.827989	0.364325	-811.44197	-811.50846	-812.21797	-812.19793
int2-c2	-811.820702	0.364306	-811.43435	-811.502244	-812.2152	-812.1903
ts2	-811.820847	0.363704	-811.43568	-811.502244	-812.21374	-812.18974
int3	-811.840226	0.365772	-811.45287	-811.519828	-812.22781	-812.2043
int3n	-812.112396	0.366062	-811.72494	-811.791592	-812.44141	-812.42075
int1'	-811.830818	0.361768	-811.44565	-811.516213	-812.2224	-812.2011
ts1'	-811.819644	0.362084	-811.4353	-811.503838	-812.2087	-812.1845
int2'	-811.828386	0.364445	-811.44207	-811.509328	-812.2171	-812.1934
ts2'	-811.820275	0.36361	-811.43523	-811.501806	-812.2145	-812.1908

int3'	-811.835024	0.365927	-811.44761	-811.514395	-812.2244	-812.2019
int3'n	-812.107687	0.367099	-811.71966	-811.784291	-812.4374	-812.4175
ts1'-c2	-811.819856	0.362392	-811.43541	-811.503368	-812.2088	-812.1851
int2'-c2	-811.826467	0.364267	-811.44032	-811.507619	-812.2142	-812.1906
ts1'-c3	-811.817539	0.363326	-811.43235	-811.499952	-812.2055	-812.1814
ts2'-c2	-811.823048	0.364276	-811.4376	-811.503233	-812.2148	-812.1918
ts1-g1	-811.809343	0.36205	-811.42516	-811.493286	-812.20077	-812.17717
ts1-g1-c2	-811.806243	0.361937	-811.42217	-811.490302	-812.19741	-812.17262
int3-g1	-811.831003	0.365911	-811.44365	-811.510568	-812.22339	-812.2003
int3n-g1	-812.10813	0.366794	-811.7204	-811.785243	-812.43726	-812.41714
ts1-g2	-811.807979	0.362206	-811.4238	-811.491482	-812.19861	-812.17524
ts1-g2-c2	-811.807962	0.362225	-811.42389	-811.490853	-812.19733	-812.17567
int3-g2	-811.836531	0.365899	-811.44902	-811.516229	-812.22909	-812.20503
int3n-g2	-812.112681	0.365856	-811.72627	-811.79125	-812.44314	-812.42185
Pathways for reaction P2:						
int6	-811.827255	0.362165	-811.44194	-811.511825	-812.2197	-812.1982
ts6	-811.8138	0.36304	-811.42878	-811.496384	-812.2023	-812.1785
int7	-811.821458	0.364966	-811.43464	-811.501867	-812.2103	-812.1865
ts6-c2	-811.811556	0.363612	-811.42618	-811.493393	-812.2	-812.1763
ts7	-811.81425	0.364527	-811.42861	-811.494203	-812.2074	-812.1843
int8	-811.829942	0.366245	-811.44256	-811.508156	-812.2191	-812.1968
int8n	-812.103398	0.367212	-811.71538	-811.779767	-812.4319	-812.4125
int6'	-811.827223	0.362287	-811.44177	-811.51156	-812.2202	-812.1994
ts6'	-811.816034	0.363552	-811.43102	-811.496903	-812.2056	-812.1854
int7'	-811.82257	0.364928	-811.43621	-811.501884	-812.2118	-812.192
ts6'-c2	-811.8122	0.363485	-811.42696	-811.49451	-812.201	-812.176
ts6'-c3	-811.8122	0.363485	-811.42696	-811.49451	-812.201	-812.176

ts7'	-811.813519	0.364032	-811.42817	-811.494741	-812.2074	-812.183
int8'	-811.834061	0.366916	-811.44593	-811.512015	-812.226	-812.203
int8'n	-812.110728	0.367118	-811.7227	-811.787491	-812.4403	-812.4199
ts6-g1	-811.806884	0.362328	-811.42258	-811.490317	-812.19768	-812.17447
ts6-g1-c2	-811.801209	0.362155	-811.41696	-811.485182	-812.18942	-812.1657
int8-g1	-811.830732	0.366015	-811.44326	-811.510872	-812.22269	-812.19944
int8n-g1	-812.106868	0.366968	-811.7188	-811.784102	-812.43678	-812.4161
ts6-g2	-811.806139	0.363078	-811.42138	-811.488039	-812.1959	-812.17399
ts6-g2-c2	-811.8041	0.362342	-811.41965	-811.487872	-812.1943	-812.1705
int8-g2	-811.833643	0.365939	-811.44623	-811.512945	-812.22535	-812.20233
int8n-g2	-812.109777	0.366958	-811.72185	-811.786849	-812.43932	-812.41901
Rotational barriers:						
ts-rot12	-811.812362	0.364997	-811.42647	-811.491979	-812.2048	-812.1799
ts-rot12'	-811.8152	0.364531	-811.4296	-811.495939	-812.2058	-812.181

Table S5. Absolute values (in Hartrees) for SCF energy, zero-point vibrational energy (ZPE), enthalpy and quasi-harmonic Gibbs free energy (at 363K) for the SET-catalysed cyclobutanation. Suffix “n” in the structure names denotes neutral species and “ra” denotes radical anionic species. Unless otherwise stated, all other species are radical cationic.

Structure	E/au	ZPE/au	qh-G/au	SP DFT (Gas)	SP DFT (MeCN)	SP DFT (HFIP)
DMP_n	-1115.8415	0.249938	-1115.645008	-1402.6497	-1402.735629	-1402.662437
DMP_ra	-1115.7557	0.252638	-1115.554097	-1402.5603	-1402.591708	-1402.510992
DMP-HFIP-c1-n	-1905.3042	0.319248	-1905.047433	-2192.4754	-2192.50852	-2192.435681
DMP-HFIP-c2-n	-1905.3081	0.319648	-1905.051909	-2192.4767	-2192.509908	-2192.433998

DMP-HFIP-c3-n	-1905.3028	0.31946	-1905.045414	-2192.4739	-2192.506098	-2192.432855
DMP-HFIP-c1-ra	-1905.4107	0.31622	-1905.158921	-2192.5846	-2192.66665068	-2192.59654685
DMP-HFIP-c2-ra	-1905.4102	0.315455	-1905.159481	-2192.5849	-2192.664661	-2192.590111
DMP-HFIP-c3-ra	-1905.4012	0.317208	-1905.149579	-2192.573	-2192.654953	-2192.58903
1a	-463.27534	0.196779	-463.113618	-463.45868	-463.4721597	-463.4554562
[1a]⁺⁺	-463.0091	0.196496	-462.848486	-463.18621	-463.269012	-463.2493934
1b	-348.79753	0.163449	-348.665962	-348.93216	-348.944163	-348.9347091
[1b]⁺⁺	-348.50864	0.162615	-348.378687	-348.63677	-348.725076	-348.7132694
2a	-463.27289	0.197361	-463.110068	-463.456269	-463.469190	-463.453090
[2a]⁺⁺	-463.00266	0.197471	-462.840538	-463.179469	-463.262410	-463.243020
2b	-348.79484	0.16385	-348.662328	-348.92946	-348.9408965	-348.9320263
[2b]⁺⁺	-348.50186	0.163047	-348.371138	-348.62965	-348.7182068	-348.7067152
int3n	-812.1124	0.366062	-811.791592	-812.42116	-812.4414079	-812.4207518
int3	-811.84023	0.365772	-811.519828	-812.14329	-812.2278126	-812.2042962
int3'_n	-812.10769	0.367099	-811.784291	-812.41664	-812.4374111	-812.4174909
int3'	-811.83502	0.365927	-811.514395	-812.1385	-812.2244248	-812.201946
int8n	-812.1034	0.367212	-811.779767	-812.41193	-812.4319308	-812.4124822
int8	-811.82994	0.366245	-811.508156	-812.13287	-812.219123	-812.1967713
int8'_n	-812.11073	0.367118	-811.787491	-812.41938	-812.4402696	-812.4199394
int8'	-811.83406	0.366916	-811.512015	-812.13712	-812.2260384	-812.2029563

Table S6. Absolute values (in Hartrees) used for redox potential calculation. SP (gas) denotes gas-phase correction at M06-2X/def2-TZVPP level of theory. The solvent corrections are the same as before.

7. Optimised geometries

Geometries of all optimized structures (in .xyz format with their associated energy in Hartrees) are included in a separate folder named *ESI_structures_xyz* with an associated README file. All these data have been deposited with this Supporting Information and uploaded to zenodo.org (DOI: 10.5281/zenodo.3946825).

8. References

Full reference for *Gaussian 09* software:

Gaussian 09, Revision D.01, M. J. Frisch, G. W. Trucks, H. B. Schlegel, G. E. Scuseria, M. A. Robb, J. R. Cheeseman, G. Scalmani, V. Barone, G. A. Petersson, H. Nakatsuji, X. Li, M. Caricato, A. Marenich, J. Bloino, B. G. Janesko, R. Gomperts, B. Mennucci, H. P. Hratchian, J. V. Ortiz, A. F. Izmaylov, J. L. Sonnenberg, D. Williams-Young, F. Ding, F. Lipparini, F. Egidi, J. Goings, B. Peng, A. Petrone, T. Henderson, D. Ranasinghe, V. G. Zakrzewski, J. Gao, N. Rega, G. Zheng, W. Liang, M. Hada, M. Ehara, K. Toyota, R. Fukuda, J. Hasegawa, M. Ishida, T. Nakajima, Y. Honda, O. Kitao, H. Nakai, T. Vreven, K. Throssell, J. A. Montgomery, Jr., J. E. Peralta, F. Ogliaro, M. Bearpark, J. J. Heyd, E. Brothers, K. N. Kudin, V. N. Staroverov, T. Keith, R. Kobayashi, J. Normand, K. Raghavachari, A. Rendell, J. C. Burant, S. S. Iyengar, J. Tomasi, M. Cossi, J. M. Millam, M. Klene, C. Adamo, R. Cammi, J. W. Ochterski, R. L. Martin, K. Morokuma, O. Farkas, J. B. Foresman, and D. J. Fox. Gaussian, Inc., Wallingford CT, 2009.

Full reference for *Q-Chem* software:

Y. Shao, Z. Gan, E. Epifanovsky, A. T. B. Gilbert, M. Wormit, J. Kussmann, A. W. Lange, A. Behn, J. Deng, X. Feng, D. Ghosh, M. Goldey, P. R. Horn, L. D. Jacobson, I. Kaliman, R. Z. Khaliullin, T. Kús, A. Landau, J. Liu, E. I. Proynov, Y. M. Rhee, R. M. Richard, M. A. Rohrdanz, R. P. Steele, E. J. Sundstrom, H. L. Woodcock III, P. M. Zimmerman, D. Zuev, B. Albrecht, E. Alguire, B. Austin, G. J. O. Beran, Y. A. Bernard, E. Berquist, K. Brandhorst, K. B. Bravaya, S. T. Brown, D. Casanova, C.-M. Chang, Y. Chen, S. H. Chien, K. D. Closser, D. L. Crittenden, M. Diedenhofen, R. A. DiStasio Jr., H. Dop, A. D. Dutoi, R. G. Edgar, S. Fatehi, L. Fusti-Molnar, A. Ghysels, A. Golubeva-Zadorozhnaya, J. Gomes, M. W. D. Hanson-Heine, P. H. P. Harbach, A. W. Hauser, E. G. Hohenstein, Z. C. Holden, T.-C. Jagau, H. Ji, B. Kaduk, K. Khistyayev, J. Kim, J. Kim, R. A. King, P. Klunzinger, D. Kosenkov, T. Kowalczyk, C. M. Krauter, K. U. Lao, A. Laurent, K. V. Lawler, S. V. Levchenko, C. Y. Lin, F. Liu, E. Livshits, R. C. Lochan, A. Luenser, P. Manohar, S. F. Manzer, S.-P. Mao, N. Mardirossian, A. V. Marenich, S. A. Maurer, N. J. Mayhall, C. M. Oana, R. Olivares-Amaya, D. P. O'Neill, J. A. Parkhill, T. M. Perrine, R. Peverati, P. A. Pieniazek, A. Prociuk, D. R. Rehn, E. Rosta, N. J. Russ, N. Sergueev, S. M. Sharada, S. Sharma, D. W. Small, A. Sodt, T. Stein, D. Stück, Y.-C. Su, A. J. W. Thom, T. Tsuchimochi, L. Vogt, O. Vydrov, T. Wang, M. A. Watson, J. Wenzel, A. White, C. F. Williams, V. Vanovschi, S. Yeganeh, S. R. Yost, Z.-Q. You, I. Y. Zhang, X. Zhang, Y. Zhou, B. R. Brooks, G. K. L. Chan, D. M. Chipman, C. J. Cramer, W. A. Goddard III, M. S. Gordon, W. J. Hehre, A. Klamt, H. F. Schaefer III, M. W. Schmidt, C. D. Sherrill, D. G. Truhlar, A. Warshel,

X. Xua, A. Aspuru-Guzik, R. Baer, A. T. Bell, N. A. Besley, J.-D. Chai, A. Dreuw, B. D. Dunietz, T. R. Furlani, S. R. Gwaltney, C.-P. Hsu, Y. Jung, J. Kong, D. S. Lambrecht, W. Liang, C. Ochsenfeld, V. A. Rassolov, L. V. Slipchenko, J. E. Subotnik, T. Van Voorhis, J. M. Herbert, A. I. Krylov, P. M. W. Gill, and M. Head-Gordon. *Advances in molecular quantum chemistry contained in the Q-Chem 4 program package*. [[Mol. Phys. 113, 184–215 \(2015\)](#)]

- (1) Frisch, M. J.; Trucks, G. W.; Schlegel, H. B.; Scuseria, G. E.; Robb, M. A.; Cheeseman, J. R.; Scalmani, G.; Barone, V.; Mennucci, B.; Petersson, G. A.; et al. Gaussian 09 Revision D.01.
- (2) Zhao, Y.; Truhlar, D. G. The M06 Suite of Density Functionals for Main Group Thermochemistry, Thermochemical Kinetics, Noncovalent Interactions, Excited States, and Transition Elements: Two New Functionals and Systematic Testing of Four M06-Class Functionals and 12 Other Function. *Theor. Chem. Acc.* **2008**, *120* (1), 215–241.
- (3) Ditchfield, R.; Hehre, W. J.; Pople, J. A. Self-Consistent Molecular-Orbital Methods. IX. An Extended Gaussian-Type Basis for Molecular-Orbital Studies of Organic Molecules. *J. Chem. Phys.* **2004**, *54* (2), 724–728.
- (4) Hay, P. J.; Wadt, W. R. Ab Initio Effective Core Potentials for Molecular Calculations. Potentials for K to Au Including the Outermost Core Orbitals. *J. Chem. Phys.* **1985**, *82* (1), 299–310.
- (5) Fukui, K. The Path of Chemical Reactions - The IRC Approach. *Acc. Chem. Res.* **1981**, *14* (12), 363–368.
- (6) Fukui, K. Formulation of the Reaction Coordinate. *J. Phys. Chem.* **2005**, *74* (23), 4161–4163.
- (7) Schäfer, A.; Horn, H.; Ahlrichs, R. Fully Optimized Contracted Gaussian Basis Sets for Atoms Li to Kr. *J. Chem. Phys.* **1992**, *97* (4), 2571–2577.
- (8) Schäfer, A.; Huber, C.; Ahlrichs, R. Fully Optimized Contracted Gaussian Basis Sets of Triple Zeta Valence Quality for Atoms Li to Kr. *J. Chem. Phys.* **1994**, *100* (8), 5829–5835.
- (9) Weigend, F.; Ahlrichs, R. Balanced Basis Sets of Split Valence, Triple Zeta Valence and Quadruple Zeta Valence Quality for H to Rn: Design and Assessment of Accuracy. *Phys. Chem. Chem. Phys.* **2005**, *7* (18), 3297–3305.
- (10) Marenich, A. V.; Cramer, C. J.; Truhlar, D. G. Universal Solvation Model Based on Solute Electron Density and on a Continuum Model of the Solvent Defined by the Bulk Dielectric Constant and Atomic Surface Tensions. *J. Phys. Chem. B* **2009**, *113* (18), 6378–6396.
- (11) Colomer, I.; Chamberlain, A. E. R.; Haughey, M. B.; Donohoe, T. J. Hexafluoroisopropanol as a Highly Versatile Solvent. *Nat. Rev. Chem.* **2017**, *1* (11), 0088.
- (12) Colomer, I.; Batchelor-Mcauley, C.; Odell, B.; Donohoe, T. J.; Compton, R. G. Hydrogen Bonding to Hexafluoroisopropanol Controls the Oxidative Strength of Hypervalent Iodine Reagents. *J. Am. Chem. Soc.* **2016**, *138* (28), 8855–8861.
- (13) Ebersson, L.; Hartshorn, M. P.; Persson, O.; Radner, F. Making Radical Cations Live Longer. *Chem. Commun.* **1996**, No. 18, 2105–2112.
- (14) Colomer, I.; Coura Barcelos, R.; Donohoe, T. J. Catalytic Hypervalent Iodine Promoters Lead to Styrene Dimerization and the Formation of Tri- and Tetrasubstituted

- Cyclobutanes. *Angew. Chem. Int. Ed.* **2016**, *55* (15), 4748–4752.
- (15) Gu, X.; Song, X.; Shao, C.; Zeng, P.; Lu, X.; Shen, X.; Yang, Q. Electrospinning of Poly(Butylene-Carbonate): Effect of Solvents on the Properties of the Nanofibers Film. *Int. J. Electrochem. Sci.* **2014**, *9* (12), 8045–8056.
- (16) Carraro, M.; Gardan, M.; Sartorel, A.; Maccato, C.; Bonchio, M. Hydrogen Peroxide Activation by Fluorophilic Polyoxotungstates for Fast and Selective Oxygen Transfer Catalysis. *Dalt. Trans.* **2016**, *45* (37), 14544–14548.
- (17) Sigma-Aldrich. 1,1,1,3,3,3-Hexafluoro-2-propanol <https://www.sigmaaldrich.com/catalog/product/aldrich/105228> (accessed Jun 6, 2017).
- (18) Weast, R. C. *CRC Handbook of Chemistry and Physics*, 76th ed.; CRC Press: Boca Raton, FL, 1995.
- (19) Richmond, E.; Yi, J.; Vuković, V. D.; Sajadi, F.; Rowley, C. N.; Moran, J. Ring-Opening Hydroarylation of Monosubstituted Cyclopropanes Enabled by Hexafluoroisopropanol. *Chem. Sci.* **2018**, *9* (30), 6411–6416.
- (20) Grimme, S. Supramolecular Binding Thermodynamics by Dispersion-Corrected Density Functional Theory. *Chem.: Eur. J.* **2012**, *18* (32), 9955–9964.
- (21) Funes-Ardoiz, I.; Paton, R. S. GoodVibes v1.0.1 <http://doi.org/10.5281/zenodo.56091>.
- (22) Horn, P. R.; Mao, Y.; Head-Gordon, M. Probing Non-Covalent Interactions with a Second Generation Energy Decomposition Analysis Using Absolutely Localized Molecular Orbitals. *Phys. Chem. Chem. Phys.* **2016**, *18* (33), 23067–23079.
- (23) Shao, Y.; Gan, Z.; Epifanovsky, E.; Gilbert, A. T. B.; Wormit, M.; Kussmann, J.; Lange, A. W.; Behn, A.; Deng, J.; Feng, X.; et al. Advances in Molecular Quantum Chemistry Contained in the Q-Chem 4 Program Package. *Mol. Phys.* **2015**, *113* (2), 184–215.
- (24) Contreras-García, J.; Johnson, E. R.; Keinan, S.; Chaudret, R.; Piquemal, J. P.; Beratan, D. N.; Yang, W. NCIPLOT: A Program for Plotting Noncovalent Interaction Regions. *J. Chem. Theory Comput.* **2011**, *7* (3), 625–632.
- (25) Schrödinger, L. *The PyMOL Molecular Graphics Development Component, Version 1.8*; 2015.
- (26) Ho, J. Are Thermodynamic Cycles Necessary for Continuum Solvent Calculation of PK a s and Reduction Potentials? *Phys. Chem. Chem. Phys.* **2015**, *17* (4), 2859–2868.
- (27) Marenich, A. V.; Ho, J.; Coote, M. L.; Cramer, C. J.; Truhlar, D. G. Computational Electrochemistry: Prediction of Liquid-Phase Reduction Potentials. *Phys. Chem. Chem. Phys.* **2014**, *16* (29), 15068–15106.
- (28) Roth, H. G.; Romero, N. A.; Nicewicz, D. A.; Roth, H. G.; Romero, N. A.; Nicewicz, D. A.; Roth, H. G.; Romero, N. A.; Nicewicz, D. A. Experimental and Calculated Electrochemical Potentials of Common Organic Molecules for Applications to Single-Electron Redox Chemistry. *Synlett* **2016**, *27* (05), 714–723.
- (29) Pavlishchuk, V. V.; Addison, A. W. Conversion Constants for Redox Potentials Measured versus Different Reference Electrodes in Acetonitrile Solutions at 25°C. *Inorganica Chim. Acta* **2000**, *298* (1), 97–102.
- (30) Isse, A. A.; Gennaro, A. Absolute Potential of the Standard Hydrogen Electrode and the Problem of Interconversion of Potentials in Different Solvents. *J. Phys. Chem. B* **2010**, *114* (23), 7894–7899.
- (31) Schröckeneder, A.; Stichnoth, D.; Mayer, P.; Trauner, D. The Crystal Structure of the Dess–Martin Periodinane. *Beilstein J. Org. Chem.* **2012**, *8* (1), 1523–1527.
- (32) Shahi, A.; Arunan, E. Microwave Spectroscopic and Theoretical Investigations of the

- Strongly Hydrogen Bonded Hexafluoroisopropanol···water Complex. *Phys. Chem. Chem. Phys.* **2015**, *17* (38), 24774–24782.
- (33) Schaal, H.; Häber, T.; Suhm, M. A. Hydrogen Bonding in 2-Propanol. The Effect of Fluorination. *J. Phys. Chem. A* **2000**, *104* (2), 265–274.
- (34) Ess, D. H.; Houk, K. N. Distortion/Interaction Energy Control of 1,3-Dipolar Cycloaddition Reactivity. *J. Am. Chem. Soc.* **2007**, *129* (35), 10646–10647.
- (35) Bickelhaupt, F. M.; Houk, K. N. Analyzing Reaction Rates with the Distortion/Interaction-Activation Strain Model. *Angew. Chem. Int. Ed.* **2017**, *56* (34), 10070–10086.
- (36) Bickelhaupt, F. M. Understanding Reactivity with Kohn-Sham Molecular Orbital Theory: E2-SN2 Mechanistic Spectrum and Other Concepts. *J. Comput. Chem.* **1999**, *20* (1), 114–128.
- (37) Fernández, I.; Bickelhaupt, F. M. The Activation Strain Model and Molecular Orbital Theory: Understanding and Designing Chemical Reactions. *Chem. Soc. Rev.* **2014**, *43* (14), 4953–4967.
- (38) Wolters, L. P.; Bickelhaupt, F. M. The Activation Strain Model and Molecular Orbital Theory. *Wiley Interdiscip. Rev. Comput. Mol. Sci.* **2015**, *5* (4), 324–343.
- (39) Marcus, R. A. On the Theory of Oxidation-Reduction Reactions Involving Electron Transfer. I. *J. Chem. Phys.* **1956**, *24* (5), 966–978.
- (40) Marcus, R. A. On the Theory of Oxidation-Reduction Reactions Involving Electron Transfer. III. Applications to Data on the Rates of Organic Redox Reactions. *J. Chem. Phys.* **1957**, *26* (4), 872–877.
- (41) Marcus, R. On the Theory of Oxidation-Reduction Reactions Involving Electron Transfer V. Comparison and Properties of Electrochemical and Chemical Rate Constants - Correction. *J. Phys. Chem.* **2007**, *67* (12), 2889–2889.
- (42) Hush, N. S. Homogeneous and Heterogeneous Optical and Thermal Electron Transfer. *Electrochim. Acta* **1968**, *13* (5), 1005–1023.
- (43) PubChem Acetonitrile <https://pubchem.ncbi.nlm.nih.gov/compound/Acetonitrile> (accessed Jun 6, 2017).
- (44) Closs, G. L.; Calcaterra, L. T.; Green, N. J.; Penfield, K. W.; Miller, J. R. Distance, Stereoelectronic Effects, and the Marcus Inverted Region in Intramolecular Electron Transfer in Organic Radical Anions. *J. Phys. Chem.* **1986**, *90* (16), 3673–3683.
- (45) Han, C. C.; Wilbur, J. L.; Brauman, J. I. Kinetic Models for Gas-Phase Electron-Transfer Reactions between Nitrobenzenes. *J. Am. Chem. Soc.* **1992**, *114* (3), 887–893.
- (46) Shannon, C. F.; Eads, D. D. Diffusion-Controlled Electron Transfer Reactions: Subpicosecond Fluorescence Measurements of Coumarin 1 Quenched by Aniline and N,N-Dimethylaniline. *J. Chem. Phys.* **1995**, *103* (13), 5208–5223.
- (47) Eyler, J. R.; Richardson, D. E. Gas-Phase Electron Transfer: Direct Observation of Kinetic Barriers in Metallocene Self-Exchange Reactions. *J. Am. Chem. Soc.* **2005**, *107* (21), 6130–6131.
- (48) Richardson, D. E. Potential Surfaces for Gas-Phase Electron-Transfer Reactions. *J. Phys. Chem.* **1986**, *90* (16), 3697–3700.
- (49) Richardson, D. E.; Christ, C. S.; Sharpe, P.; Eyler, J. R. Gas-Phase Electron Transfer: Thermal Self-Exchange and Cross Reactions of Organometallic Molecules and Ions. *J. Am. Chem. Soc.* **1987**, *109* (13), 3894–3902.